Progress of Theoretical Physics, Vol. 101, No. 6, June 1999

Fully General Relativistic Simulation of Merging Binary Clusters

—— *Spatial Gauge Condition* ——

Masaru Shibata

Department of Physics, University of Illinois at Urbana-Champaign
Urbana, IL 61801, USA
and
Department of Earth and Space Science, Graduate School of Science
Osaka University, Toyonaka 560-0043, Japan

(Received March 19, 1999)

We have carried out simulations of the coalescence between two relativistic clusters of collisionless particles using a 3D numerical relativity code. We have adopted a new spatial gauge condition obtained by slightly modifying the minimum distortion gauge condition proposed by Smarr and York and resulting in a simpler equation for the shift vector. Using this gauge condition, we have performed several simulations of the merger between two identical clusters in which we have varied the compaction, the type of internal motion in the clusters, and the magnitude of the orbital velocity. As a result of the coalescence, either a new rotating cluster or a black hole is formed. In the case in which a black hole is not formed, simulations could be carried out for a time much longer than the dynamical time scale, and the resulting gravitational waveforms were calculated fairly accurately: In these cases, the amplitude of gravitational waves emitted can be $\sim 10^{-18}(M/10^6\,M_\odot)$ at a distance 4000 Mpc, and $\sim 0.5\%$ of the rest mass energy may be dissipated by the gravitational wave emission in the final phase of the merger. These results confirm that the new spatial gauge condition is promising in many problems at least up to the formation of black holes. In the case in which a black hole is formed, on the other hand, the gauge condition seems to be less adequate, but we suggest a strategy to improve it in this case. All of the results obtained confirm the robustness of our formulation and the ability of our code for stable evolution of strong gravitational fields of compact binaries.

§1. Introduction

The coalescences of relativistic binaries are the most promising sources for kilometer-size laser interferometers such as LIGO,[1),2)] VIRGO,[3)] GEO[4)] and TAMA,[5)] which will be in operation in the next five years, as well as for future space-based interferometric gravitational wave detectors such as LISA.[6)] When a signal of gravitational waves from such compact objects is detected, it will be analyzed using matched filter techniques, and a variety of astrophysical information will be extracted.[2)] In order to apply this technique, theoretical templates of gravitational waveforms will be needed, and this motivates the recent theoretical study of gravitational waves emitted from coalescing binaries. The post-Newtonian approximation has been shown to be a powerful tool for the study of the inspiraling phase, and a large effort devoted to this study has produced many satisfactory results.[7)] However, in order to study the final phase of the coalescence, in which strong general relativistic effects dominate, no approximation of general relativity is valid, and 3D

numerical relativistic simulations appear to be the only promising approach.

Although a few results have been obtained recently,[8] there are still a number of fundamental questions that need to be addressed. Among them, it is particularly important and urgent to find appropriate gauge conditions which allow one to perform stable simulations and to extract gravitational waves accurately. As shown by many numerical simulations, the maximal slice condition seems to be an adequate time slice condition at least up to the formation of black holes. However, a similarly reliable spatial gauge condition in 3D numerical relativity has not yet been studied sufficiently. More than 20 years ago, Smarr and York[9] proposed a minimum distortion (MD) gauge condition, which is expected to have several excellent mathematical properties. From a numerical point of view, however, the MD gauge condition requires the solution of a complicated vector elliptic equation, and this can be a very time-consuming task.

Their MD gauge condition was contrived from the idea that the global change rate of the conformal spatial metric should be minimized.[9] This is a rather restrictive condition, and we believe that a gauge condition in which the global change rate is not *exactly* minimized but instead only *approximately* minimized can prove to be appropriate, as long as the geometrical distortion of the three space does not increase quickly. Thus, in this paper, we propose an approximate minimum distortion (AMD) gauge condition which is similar to Smarr and York's MD gauge condition and in which the global change rate is expected to be only approximately minimized. In a numerical simulation, the AMD gauge condition is much more easily imposed than the original MD gauge condition.

In a previous paper,[10] we presented results from numerical simulations of black hole formation in which collisionless particles were used as matter sources of the Einstein equation. That study demonstrated that our formulation is robust, that it allows for stable numerical evolution, and that it can be applied to problems such as the formation of black holes from collision of two clusters, or gravitational collapse. In this paper, we use our code to simulate the merger between two identical binary clusters, adopting an AMD gauge condition, and we demonstrate that this formulation with a new spatial gauge condition allows for stable numerical evolutions of merging binaries and for fairly accurate calculation of gravitational waves.

Numerical simulations of the merger between relativistic clusters may become a source of important information in astrophysics and gravitational wave astronomy. It has been in fact proposed that supermassive black holes in galactic centers might be formed through complex phenomena such as gravitational collapse and bar instability, involving the coalescence between clusters of collisionless compact stars.[11] If such phenomena occurred frequently in the early universe, they could have produced low frequency gravitational waves which would be detected by the planned interferometric detectors in space.[6] In particular, the coalescence of two compact clusters could be an important source. The simulation presented in this paper may play a role in predicting the amplitude and frequency of the gravitational waves emitted during such coalescences.

The paper is organized as follows. In §2, we present the basic equations to be solved in the numerical simulation. In §3, we describe the spatial AMD gauge

condition adopted in this paper and briefly discuss its properties. In §4, we describe the methods employed in order to analyze the gravitational waves radiated. In §5, after we briefly describe the method to set the initial conditions, we present numerical results for simulations of the coalescence of two clusters. Section 6 is devoted to summary. Throughout this paper, we adopt units in which $G = 1 = c$. Latin and Greek indices denote spatial components $(1-3)$ and spacetime components $(0-3)$, respectively. As spatial coordinates, we use the Cartesian coordinates $x^k = (x, y, z)$ with $r = \sqrt{x^2 + y^2 + z^2}$.

§2. Basic equations

Our formulation of the Einstein equation is described in detail in previous papers.[12),10)] We here briefly recall the basic equations and refer the reader to the above cited works for details.

We write the line element in the form

$$ds^2 = (-\alpha^2 + \beta_k\beta^k)dt^2 + 2\beta_i dx^i dt + \gamma_{ij}dx^i dx^j, \tag{2·1}$$

where α, β^i ($\beta_i = \gamma_{ij}\beta^j$) and γ_{ij} are the lapse function, shift vector and 3D spatial metric, respectively. We define the quantities

$$\gamma = \det(\gamma_{ij}) \equiv e^{12\phi}, \tag{2·2}$$

$$\tilde{\gamma}_{ij} \equiv e^{-4\phi}\gamma_{ij}, \text{ i.e., } \det(\tilde{\gamma}_{ij}) = 1, \tag{2·3}$$

$$\tilde{A}_{ij} \equiv e^{-4\phi}\left(K_{ij} - \frac{1}{3}\gamma_{ij}K\right), \tag{2·4}$$

where K_{ij} is the extrinsic curvature, and $K = K_k{}^k$. The indices of $\tilde{A}_{ij}$ and/or $\tilde{A}^{ij}$ are raised and lowered in terms of $\tilde{\gamma}_{ij}$ and $\tilde{\gamma}^{ij}$. Numerical computations are carried out using $\tilde{\gamma}_{ij}$, $\tilde{A}_{ij}$, ϕ and K as dynamical variables rather than γ_{ij} and K_{ij}. Hereafter, we use D_i and $\tilde{D}_i$ as the covariant derivatives with respect to γ_{ij} and $\tilde{\gamma}_{ij}$, respectively.

Since our matter source is represented by collisionless particles, its energy momentum tensor is written as

$$T_{\mu\nu} = m_p \sum_{a=1}^{N} \frac{\delta^{(3)}(x^j - x_a^j)}{\alpha e^{6\phi}} \left(\frac{u_\mu u_\nu}{u^0}\right)_a, \tag{2·5}$$

where m_p is the rest mass of each particle (we assume that all particles have the same rest mass), x_a^j denotes the position of the a-th particle, N is the total particle number, u_μ is the four-velocity of a particle, and $\delta^{(3)}(x^j - x_a^j)$ is the Dirac delta function in the 3D spatial hypersurface. Note that the rest mass density ρ_* and the total rest mass (i.e., conserved mass) M_* are written as

$$\rho_* = m_p \sum_{a=1}^{N} \delta^{(3)}(x^j - x_a^j), \tag{2·6}$$

$$M_* = 4Nm_p, \tag{2·7}$$

where the factor 4 in Eq. (2·7) arises because in this paper we assume a plane symmetry with respect to the equatorial plane ($z = 0$) as well as a π-rotation symmetry around the z-axis, and treat only a quadrant region (see below).

The equations of motion for the particles are derived from the geodesic equations and are written in the form

$$\frac{du_i}{dt} = -\alpha u^0 \alpha_{,i} + u_j \beta^j{}_{,i} - \frac{u_j u_k}{2u^0}\gamma^{jk}{}_{,i} \quad , \tag{2·8}$$

where $Q_{,j} = \partial_j Q = \partial Q/\partial x^j$. Once u_i is obtained, u^0 is determined from the normalization relation of the four-velocity as

$$(\alpha u^0)^2 = 1 + \gamma^{ij} u_i u_j \quad . \tag{2·9}$$

We also have a relation between a coordinate velocity $dx^i/dt \equiv u^i/u^0$ and u_j as

$$\frac{dx^i}{dt} = -\beta^i + \frac{\gamma^{ij} u_j}{u^0} \quad . \tag{2·10}$$

Equations (2·8) and (2·10) are the basic equations for evolution of the particle's position and velocity.

As customary in a 3+1 decomposition, the Einstein equation is split into the constraint and evolution equations. The Hamiltonian and momentum constraint equations are given by

$$R - \tilde{A}_{ij}\tilde{A}^{ij} + \frac{2}{3}K^2 = 16\pi E, \tag{2·11}$$

$$D_i \tilde{A}^i{}_j - \frac{2}{3} D_j K = 8\pi J_j, \tag{2·12}$$

where

$$E = m_p \sum_{a=1}^{N} (u^0)_a \alpha e^{-6\phi} \delta^{(3)}(x^k - x^k_a), \tag{2·13}$$

$$J_i = m_p \sum_{a=1}^{N} (u_i)_a e^{-6\phi} \delta^{(3)}(x^k - x^k_a), \tag{2·14}$$

and R is the scalar curvature with respect to γ_{ij}. We solve these constraint equations only when setting initial conditions.

The evolution equations for the geometric variables $\tilde{\gamma}_{ij}$, ϕ, $\tilde{A}_{ij}$ and K are given by [10]

$$(\partial_t - \beta^k \partial_k)\tilde{\gamma}_{ij} = -2\alpha \tilde{A}_{ij} + \tilde{\gamma}_{ik}\beta^k{}_{,j} + \tilde{\gamma}_{jk}\beta^k{}_{,i} - \frac{2}{3}\tilde{\gamma}_{ij}\beta^k{}_{,k} \quad , \tag{2·15}$$

$$\begin{aligned}(\partial_t - \beta^k \partial_k)\tilde{A}_{ij} = {} & e^{-4\phi}\left[\alpha\left(R_{ij} - \frac{1}{3}\gamma_{ij}R\right) - \left(D_i D_j \alpha - \frac{1}{3}\gamma_{ij} D_k D^k \alpha\right)\right] \\ & + \alpha(K\tilde{A}_{ij} - 2\tilde{A}_{ik}\tilde{A}_j{}^k) + \beta^k{}_{,i}\tilde{A}_{kj} + \beta^k{}_{,j}\tilde{A}_{ki} - \frac{2}{3}\beta^k{}_{,k}\tilde{A}_{ij}\end{aligned}$$

$$- 8\pi\alpha e^{-4\phi}\left(S_{ij} - \frac{1}{3}\gamma_{ij}S_k{}^k\right), \tag{2·16}$$

$$(\partial_t - \beta^k\partial_k)\phi = \frac{1}{6}\left(-\alpha K + \beta^k{}_{,k}\right), \tag{2·17}$$

$$(\partial_t - \beta^k\partial_k)K = \alpha\left(\tilde{A}_{ij}\tilde{A}^{ij} + \frac{1}{3}K^2\right) - D_kD^k\alpha + 4\pi\alpha(E + S_k{}^k), \tag{2·18}$$

where R_{ij} is the Ricci tensor with respect to γ_{ij}, and

$$S_{ij} = m_p\sum_{a=1}^{N}\left(\frac{u_iu_j}{u^0}\right)_a\frac{\delta^{(3)}(x^k - x_a^k)}{\alpha e^{6\phi}}. \tag{2·19}$$

We also solve the following equation for $F_i \equiv \delta^{jk}\tilde{\gamma}_{ij,k}$:[12),10),13)]

$$\begin{aligned}(\partial_t - \beta^k\partial_k)F_i = {} & 2\alpha\left(f^{kj}\tilde{A}_{ik,j} + f^{kj}{}_{,j}\tilde{A}_{ik} - \frac{1}{2}\tilde{A}^{jl}h_{jl,i} + 6\phi_{,k}\tilde{A}^k{}_i - \frac{2}{3}K_{,i}\right)\\ & - 2\delta^{jk}\alpha_{,k}\tilde{A}_{ij} + \delta^{jl}\beta^k{}_{,l}h_{ij,k} + (\tilde{\gamma}_{il}\beta^l{}_{,j} + \tilde{\gamma}_{jl}\beta^l{}_{,i} - \frac{2}{3}\tilde{\gamma}_{ij}\beta^l{}_{,l})_{,k}\delta^{jk}\\ & - 16\pi\alpha J_i \quad .\end{aligned} \tag{2·20}$$

Here δ_{ij} denotes the Kronecker delta, $h_{ij} = \tilde{\gamma}_{ij} - \delta_{ij}$, and $f^{ij} = \tilde{\gamma}^{ij} - \delta^{ij}$. F_i is used to compute R_{ij} and R.[10)] As argued in previous papers,[12),10)] the introduction of F_i is necessary for stable numerical computation.

As the time slice condition, we use an approximate maximal slice condition. Namely, we determine α by demanding that the right-hand side of Eq. (2·18) becomes approximately zero, using a strategy discussed in a previous paper.[10)] A discussion of the spatial gauge condition used in this paper will be presented in the next section.

The numerical methods employed in solving Eqs. (2·8), (2·10), (2·15)–(2·18) and (2·20), and for finding the apparent horizon are almost the same as those discussed in a previous paper,[10)] except for the following two differences. The first difference is due to the appearance of the transport terms such as $-\beta^k\partial_k\tilde{\gamma}_{ij}$ in the evolution equations of the geometric variables. This is because we choose a non-zero β^k (in a previous paper[10)] we adopted $\beta^k = 0$). A discussion of our strategy for handling such transport terms is described in Appendix A. The second difference is due to the different underlying symmetries assumed here. In this paper, we solve equations in the quadrant region $-L \le x \le L$, $0 \le y, z \le L$, where L denotes the location of the outer boundaries, assuming π-rotation symmetry around the z-axis as well as the plane symmetry with respect to the $z = 0$ plane (in a previous paper[10)] we assumed triplane symmetry). We note that we perform simulations of binary clusters whose mass centers orbit in the $z = 0$ plane (see §5). Boundary conditions in the $y = 0$ plane are as follows:

$$Q(x,0,z) = Q(-x,0,z), \tag{2·21}$$

$$Q^A(x,0,z) = -Q^A(-x,0,z), \quad Q_A(x,0,z) = -Q_A(-x,0,z), \tag{2·22}$$

$$Q^z(x,0,z) = Q^z(-x,0,z), \quad Q_z(x,0,z) = Q_z(-x,0,z), \tag{2·23}$$

$$Q_{AB}(x,0,z) = Q_{AB}(-x,0,z), \tag{2·24}$$

$$Q_{Az}(x,0,z) = -Q_{Az}(-x,0,z), \tag{2·25}$$
$$Q_{zz}(x,0,z) = Q_{zz}(-x,0,z), \tag{2·26}$$

where A, $B = x$ or y, and Q, Q^i(or Q_i) and Q_{ij} denote arbitrary scalar, vector and tensor quantities, respectively. Note that the boundary conditions at the outer boundaries are the same as those in a previous paper [10] except for that of F_i for which we impose $F_i = O(r^{-3})$ in this paper. It is also convenient to define the quantities

$$j(r) = m_p \sum_{a=1}^{N} (xu_y - yu_x)_a \quad \text{for } r_a < r, \tag{2·27}$$
$$m_*(r) = m_p N_p(r), \tag{2·28}$$

where $r_a = \sqrt{x_a^2 + y_a^2 + z_a^2}$ and $N_p(r)$ denotes the number of particles which are in a radius r. We consider $j(r)$ to be the approximate z-component of the angular momentum within r, while $m_*(r)$ denotes the total rest mass within r.

§3. Spatial gauge condition

The MD gauge condition proposed by Smarr and York [9] can be written as

$$D^i(e^{4\phi}\partial_t \tilde{\gamma}_{ij}) = 0, \tag{3·1}$$

or, equivalently, as

$$\tilde{D}^i(e^{6\phi}\partial_t \tilde{\gamma}_{ij}) = 0. \tag{3·2}$$

More explicitly, their MD gauge condition reduces to an equation for β^k:

$$\tilde{D}^i\Big(\tilde{D}_i\tilde{\beta}_j + \tilde{D}_j\tilde{\beta}_i - \frac{2}{3}\tilde{\gamma}_{ij}\tilde{D}_k\tilde{\beta}^k\Big) + 6\tilde{D}^i\phi\Big(\tilde{D}_i\tilde{\beta}_j + \tilde{D}_j\tilde{\beta}_i - \frac{2}{3}\tilde{\gamma}_{ij}\tilde{D}_k\tilde{\beta}^k\Big)$$
$$-2\tilde{A}_{ij}\tilde{D}^i\alpha - \frac{4}{3}\alpha\tilde{D}_j K = 16\pi\alpha J_j. \tag{3·3}$$

Here $\tilde{\beta}_k = \tilde{\gamma}_{kl}\beta^l$ and $\tilde{\beta}^k = \beta^k$. Smarr and York's MD gauge condition is also derived by minimizing the following action I with respect to β^k on three spacelike hypersurfaces: [9]

$$I = \int d^3x(\partial_t\tilde{\gamma}_{ij})(\partial_t\tilde{\gamma}_{kl})\tilde{\gamma}^{ik}\tilde{\gamma}^{jl}e^{6\phi}. \tag{3·4}$$

Thus, by choosing Smarr and York's MD gauge condition, the global change rate of $\tilde{\gamma}_{ij}$ *based on the action* I is minimized in every three hypersurface.

Since I does not have a special physical meaning, we may consider an alternative gauge condition by slightly changing the definition of the action. In particular, we define another action I' as

$$I' = \int d^3x(\partial_t\tilde{\gamma}_{ij})(\partial_t\tilde{\gamma}_{kl})\tilde{\gamma}^{ik}\tilde{\gamma}^{jl}. \tag{3·5}$$

This corresponds to defining the action in the conformal three space in which the determinant of the metric $\det(\tilde{\gamma}_{ij})$ is unity. In this case, by taking the variation of I' with respect to β^k, we obtain a different MD gauge condition,

$$\tilde{D}^i(\partial_t \tilde{\gamma}_{ij}) = 0, \tag{3·6}$$

or more explicitly,

$$\tilde{D}^i\left(\tilde{D}_i\tilde{\beta}_j + \tilde{D}_j\tilde{\beta}_i - \frac{2}{3}\tilde{\gamma}_{ij}\tilde{D}_k\tilde{\beta}^k\right) - 2\tilde{A}_{ij}(\tilde{D}^i\alpha - 6\alpha\tilde{D}^i\phi) - \frac{4}{3}\alpha\tilde{D}_j K = 16\pi\alpha J_j. \tag{3·7}$$

A merit of this condition may be that we do not have a coupling term between $\tilde{\beta}^k$ and ϕ, and hence the equation for $\tilde{\beta}^k$ is slightly simplified compared with Eq. (3·3). However, it is still complicated to solve in numerical computation.

Although it is desirable to adopt a shift vector in which I or I' is *exactly* minimized, we believe that we do not always have to use such a shift vector. We may probably use another shift vector in which I or I' is *approximately* minimized. Using this idea, we derive a gauge condition by slightly changing Eq. (3·7): We rewrite the covariant derivative operator $\tilde{D}_i$ acting on $\tilde{\beta}^k$ as a partial derivative; i.e., we solve the following equation to determine $\beta^k (= \tilde{\beta}^k)$:

$$\delta_{ij}\Delta\beta^i + \frac{1}{3}\beta^k{}_{,kj} - 2\tilde{A}_{ij}(\tilde{D}^i\alpha - 6\alpha\tilde{D}^i\phi) - \frac{4}{3}\alpha\tilde{D}_j K = 16\pi\alpha J_j. \tag{3·8}$$

Here Δ is the Laplacian in the flat space. In this case, Eq. (3·8) can be rewritten into simple elliptic equations for a vector P_i and a scalar η using the transformation

$$\beta^j = \delta^{ji}\left[\frac{7}{8}P_i - \frac{1}{8}(\eta_{,i} + P_{k,i}x^k)\right], \tag{3·9}$$

where P_i and η satisfy

$$\Delta P_i = S_i, \tag{3·10}$$

$$\Delta\eta = -S_i x^i, \tag{3·11}$$

and

$$S_i \equiv 16\pi\alpha J_i + 2\tilde{A}_{ij}(\tilde{D}^j\alpha - 6\alpha\tilde{D}^j\phi) + \frac{4}{3}\alpha\tilde{D}_i K. \tag{3·12}$$

In this way, the equation for β^k is significantly simplified and reduces to equations similar to those we have solved in the initial value problem [14] and in post-Newtonian studies. [15] Hereafter, we refer to the gauge condition presented here as an "approximate minimum distortion" (AMD) gauge.

The above described AMD gauge condition is expected to have the following properties:

- In a spherical symmetric spacetime with conformal flat initial conditions, it coincides with Smarr and York's MD gauge condition (Eq. (3·2)) as well as with the MD gauge condition presented in this paper (Eq. (3·6)), because in this case, $\tilde{\gamma}_{ij} = \delta_{ij}$ and $\partial_t\tilde{\gamma}_{ij} = 0$.

- Using a post-Newtonian approximation as a guide, we can see that the difference between our AMD gauge and the MD gauge condition defined by Eq. (3·6) appears, in general, at the third post-Newtonian order, because we neglect only coupling terms between h_{ij} (or f^{ij}) and β^k.[16),17)] Hence, this difference is in general small, and we may expect that the global change rate of $\tilde{\gamma}_{ij}$ is still suppressed and is always sufficiently small.
- As in the MD gauge conditions, in the AMD gauge condition, h_{ij} approximately satisfies a transverse relation ($F_i = 0$) everywhere except for a region near a rapidly rotating object as long as F_i is sufficiently small at $t = 0$ (see Appendix B). Thus, we expect that such gauge condition will prove useful for analyzing gravitational waves in the wave zone, in which h_{ij} approximately satisfies a transverse-traceless (TT) condition, $h_{ij}\delta^{ij} = h_{ij,k}\delta^{jk} = 0$.

In conclusion, the AMD gauge condition presented here possesses many of the merits of the MD gauge conditions, and it also results in equations which are much more easily solved numerically.

§4. Analysis of gravitational waves

In this paper, we analyze gravitational waveforms as measured by an observer located near the outer boundaries of the computational domain. Along the z-axis, this can be done through the quantities

$$h_+ \equiv r(\tilde{\gamma}_{xx} - \tilde{\gamma}_{yy})/2, \tag{4·1}$$

$$h_\times \equiv r\tilde{\gamma}_{xy}. \tag{4·2}$$

Since we adopt our AMD gauge condition and consider initial conditions with $F_i = 0$, h_{ij} is approximately TT in the wave zone. As a result, h_+ and $h_\times$ are expected to be appropriate measures of gravitational waves emitted. (See §5 for a discussion of this.) The amplitude of gravitational waves will be largest along the z-axis as a result of our construction of initial data sets (see §5.1), and therefore h_+ and $h_\times$ should be regarded as the maximum amplitude of gravitational waves.

Gravitational waves are also measured through the gauge invariant Moncrief variables in flat spacetime, which are defined as follows:[18)] First, we transform from the Cartesian coordinates to the spherical polar coordinates, and then we split γ_{ij} as $\delta_{ij} + \sum_{lm} \zeta_{ij}^{lm}$, where ζ_{ij}^{lm} denotes

$$\zeta_{ij}^{lm} = \begin{pmatrix} H_2 Y_{lm} & h_{1lm} Y_{lm,\theta} & h_{1lm} Y_{lm,\varphi} \\ & r^2(K_{lm} Y_{lm} + G_{lm} W_{lm}) & r^2 G_{lm} X_{lm} \\ & * & r^2 \sin^2\theta (K_{lm} Y_{lm} - G_{lm} W_{lm}) \end{pmatrix} + \begin{pmatrix} 0 & -C_{lm}\partial_\varphi Y_{lm}/\sin\theta & C_{lm}\partial_\theta Y_{lm}\sin\theta \\ * & r^2 D_{lm} X_{lm}/\sin\theta & -r^2 D_{lm} W_{lm}\sin\theta \\ * & * & -r^2 D_{lm} X_{lm}\sin\theta \end{pmatrix}, \tag{4·3}$$

and $*$ denotes the relation of symmetry. H_{2lm}, h_{1lm}, K_{lm}, G_{lm}, C_{lm} and D_{lm} are functions of r and t, and are calculated by performing integrations over a two sphere

of given radius (see a previous paper [12]) for detail). Y_{lm} is the spherical harmonic function, and W_{lm} and X_{lm} are defined as

$$W_{lm} \equiv \left[(\partial_\theta)^2 - \cot\theta\partial_\theta - \frac{1}{\sin^2\theta}(\partial_\varphi)^2\right]Y_{lm}, \tag{4·4}$$

$$X_{lm} \equiv 2\partial_\varphi\left[\partial_\theta - \cot\theta\right]Y_{lm}. \tag{4·5}$$

The Moncrief variables of even and odd parities are then defined as

$$R^{\rm E}_{lm}(t,r) \equiv \sqrt{\frac{2(l-2)!}{(l+2)!}}\left\{4k_{2lm} + l(l+1)k_{1lm}\right\}, \tag{4·6}$$

$$R^{\rm O}_{lm}(t,r) \equiv \sqrt{\frac{2(l+2)!}{(l-2)!}}\left(2\frac{C_{lm}}{r} + r\partial_r D_{lm}\right), \tag{4·7}$$

where

$$k_{1lm} \equiv K_{lm} + l(l+1)G_{lm} + 2r\partial_r G_{lm} - 2\frac{h_{1lm}}{r}, \tag{4·8}$$

$$k_{2lm} \equiv \frac{H_{2lm}}{2} - \frac{1}{2}\frac{\partial}{\partial r}\left[r\{K_{lm} + l(l+1)G_{lm}\}\right]. \tag{4·9}$$

Note that using the above variables, the energy luminosity of gravitational waves can be calculated as

$$\frac{dE}{dt} = \frac{r^2}{32\pi}\left[(\partial_t R^{\rm E}_{lm})^2 + (\partial_t R^{\rm O}_{lm})^2\right]. \tag{4·10}$$

In this paper, we consider only the even parity Moncrief variables of $l = |m| = 2$, which are expected to have the largest amplitude.

§5. Numerical study

We have carried out numerical simulations of the merger between two identical relativistic clusters of collisionless particles for several sets of initial conditions. In the following, we present the results obtained and demonstrate that the AMD gauge condition discussed in §3 is robust and allows us to perform simulations for a time much longer than the dynamical time scale and to extract gravitational waveforms.

5.1. *Initial conditions*

For simplicity, we use conformally flat initial conditions. In this case, we only need to solve the Hamiltonian and momentum constraint equations, in addition to the equations for α and β^k. The constraint equations are written as [10]

$$\Delta\psi = -2\pi E\psi^5 - \frac{1}{8}\hat{A}_{ij}\hat{A}^{ij}\psi^{-7}, \tag{5·1}$$

$$\hat{A}_i{}^j{}_{,j} = 8\pi J_i\psi^6, \tag{5·2}$$

where $\hat{A}_{ij} \equiv \psi^6\tilde{A}_{ij}$. As discussed in a previous paper,[10] we write $\hat{A}_{ij}$ as

$$\hat{A}_{ij} = W_{i,j} + W_{j,i} - \frac{2}{3}\delta_{ij}W_{k,l}\delta^{kl}, \tag{5·3}$$

with

$$W_i = \frac{7}{8}B_i - \frac{1}{8}\Big(\chi_{,i} + B_{k,i}x^k\Big). \tag{5·4}$$

Then, the equations for B_i and χ are derived from Eq. (5·2) as

$$\Delta B_i = 8\pi J_i\psi^6 = 8\pi\rho_* u_i, \tag{5·5}$$

$$\Delta\chi = -8\pi J_i x^i\psi^6 = -8\pi\rho_* u_i x^i. \tag{5·6}$$

As a result of Eqs. (5·3) and (5·4), Eqs. (5·1), (5·5) and (5·6) are regarded as constraint equations to be solved. The strategy for setting up initial conditions is as follows: (1) we choose $\rho_*(x,y,z)$ and $u_i(x,y,z)$; (2) we solve Eqs. (5·5) and (5·6), from which $\hat{A}_{ij}$ is subsequently obtained; (3) we solve Eq. (5·1).

The rest mass density profile $\rho_*(x,y,z)$ of each cluster is simply chosen to be a parabolic function of the type

$$\rho_*(r_\pm) = \begin{cases} \rho_0\Big(1 - \dfrac{r_\pm^2}{r_0^2}\Big) & r_\pm < r_0, \\ 0 & r_\pm \geq r_0, \end{cases} \tag{5·7}$$

where ρ_0 and r_0 are constants, and $r_\pm$ denote coordinate distances from the center of each cluster which is located at $(\pm r_c, 0, 0)$ with $r_c > r_0$.

As one model, we choose the velocity field u_i for $r_\pm < r_0$ as

$$u_i(x,y,z) = u_i^{\rm orb} = \Big(-0.01\frac{|x|}{x}V,\ \frac{|x|}{x}V,\ 0\Big), \tag{5·8}$$

where

$$V = \omega_0\sqrt{\frac{M_*^{\rm one}}{4r_c}}, \tag{5·9}$$

and $M_*^{\rm one} = 8\pi\rho_0 r_0^3/15$ is the total rest mass of one cluster. When we set the velocity field as Eq. (5·8), we always refer to the model of the initial condition as Kepler model. In this model, we choose $\omega_0 = 1$ (near Kepler angular velocity case) and 0.5. We also choose a nearly corotating velocity field as

$$u_i(x^i) = u_i^{\rm orb} = \Big(-0.01\frac{|x|}{x}V - \frac{y}{r_c}V,\ \frac{x}{r_c}V,\ 0\Big). \tag{5·10}$$

In this case, we set $\omega_0 = 1$. We refer to the model of the initial condition as corotating model.

Once ρ_* and u_i are given, we can solve the constraint equations, as well as calculate the initial z-component of the total angular momentum of the system

$$J = \int d^3x\rho_*(xu_y - yu_x) = j(\infty). \tag{5·11}$$

Since we now consider the case in which each cluster is in near equilibrium, we must determine an appropriate velocity for each particle in addition to the orbital velocity. The method to determine the velocity $(u_i)_a$ for the a-th particle is as

follows. First, we numerically solve equations for an equilibrium state of a single spherical cluster assuming that ρ_* is given by the parabolic function as Eq. (5·7). The equilibrium state is easily obtained, as we have done in a previous paper. [10] Once we obtain an equilibrium state of a spherical cluster, the square of the velocity field, $u_i^{\rm one}u_i^{\rm one} \equiv \ell^2$, is obtained as a function of the coordinate distance from the center. Then, we assign the velocity of the a-th particle at $(x_a, y_a, z_a) = (x_p \pm r_c, y_p, z_p)$ as

$$
\begin{aligned}
(u_x)_a &= \ell(r_p)\left(\frac{x_p z_p}{r_p\sqrt{x_p^2+y_p^2}}\cos\zeta - \frac{y_p}{\sqrt{x_p^2+y_p^2}}\sin\zeta\right) + u_x^{\rm orb},\\
(u_y)_a &= \ell(r_p)\left(\frac{y_p z_p}{r_p\sqrt{x_p^2+y_p^2}}\cos\zeta + \frac{x_p}{\sqrt{x_p^2+y_p^2}}\sin\zeta\right) + u_y^{\rm orb},\\
(u_z)_a &= -\ell(r_p)\frac{\sqrt{x_p^2+y_p^2}}{r_p}\cos\zeta,
\end{aligned}
\tag{5·12}
$$

where $r_p^2 = x_p^2 + y_p^2 + z_p^2$, and random numbers of uniform deviation between 0 and 2π are assigned for ζ. Namely, the velocity of each particle is written as a linear combination of the velocity obtained in constructing a single equilibrium spherical cluster and of the orbital velocity. In order to guarantee that the velocity field is given by $u_i = u_i^{\rm orb}$ at any point, we have distributed particles in an appropriate manner. Hence, in the limit $r_c \to \infty$, each cluster is in a true equilibrium.

In addition to the constraint equations, we also need to solve equations for α and β^k, where for the latter, we use the prescription discussed in the previous section. Since we require α to initially satisfy the maximal slice condition, $K = 0 = \partial_t K$, we solve the equation

$$
\Delta(\alpha\psi) = 2\pi\alpha\psi^5(E + 2S_k{}^k) + \frac{7}{8}\alpha\psi^{-7}\hat{A}_{ij}\hat{A}^{ij}, \tag{5·13}
$$

after we have a solution for $\hat{A}_{ij}$ and ψ.

5.2. *Numerical results*

All simulations were carried out fixing parameters as $r_0 = 1$ and $r_c = 1.1r_0$, but using three different values for the total rest mass $M_* = 2M_*^{\rm one}$, $r_0/6$, $r_0/4$ and $r_0/3$ (i.e., changing ρ_0). We note that in all cases, each spherical star is stable in isolation. Only when M_* is greater than $\sim r_0/2.5$, a spherical star becomes unstable in isolation for the density profile given by Eq. (5·7), because some orbits near the surface of the cluster are unstable.

We typically use a uniform grid with $(153, 77, 77)$ points and covering a coordinate domain with extents $-7.6r_0 \le x \le 7.6r_0$ and $0 \le y, z \le 7.6r_0$ (i.e., $\delta x = \delta y = \delta z = 0.1r_0$). In this case, radius of each cluster is covered by 10 grid points initially. We typically take the particle number N to be 10^5.*) Hereafter, all quantities are given in units $r_0 = 1$ (and $G = 1 = c$).

*) For some cases, we performed simulations changing N and the grid spacing, and found that the numerical results changed somewhat in particular after the collision of two clusters. This is due to the different magnitude of the fluctuations caused by the discreteness of the particle locations. However, the global features discussed here did not change considerably.

Table I. The list of initial conditions and final states for simulations performed in §5. $M_* = 2M_*^{\rm one}$, M, J and T denote the total rest mass, gravitational mass, total angular momentum and approximate initial orbital period ($2\pi\sqrt{8r_c^3/M_*}$), respectively. All the quantities are given in units $r_0 = 1$ (and $G = 1 = c$). In the cases marked with †, we could not determine the apparent horizon formation, but black holes seem to be formed.

M_*	M/M_*	J/M^2	T	velocity field	Final state	Figures
1/6	0.966	0.974	50.2	Kepler($\omega_0 = 1$)	rotating cluster	1
1/4	0.952	0.818	41.0	Kepler($\omega_0 = 1$)	rotating cluster	2, 4, 11, 13
1/3	0.941	0.726	35.5	Kepler($\omega_0 = 1$)	black hole†	3
1/4	0.955	1.01	41.0	Corotation	rotating cluster	5, 12, 14
1/3	0.944	0.894	35.5	Corotation	black hole†	6
1/3	0.931	0.371	–	Kepler($\omega_0 = 0.5$)	black hole	7–10

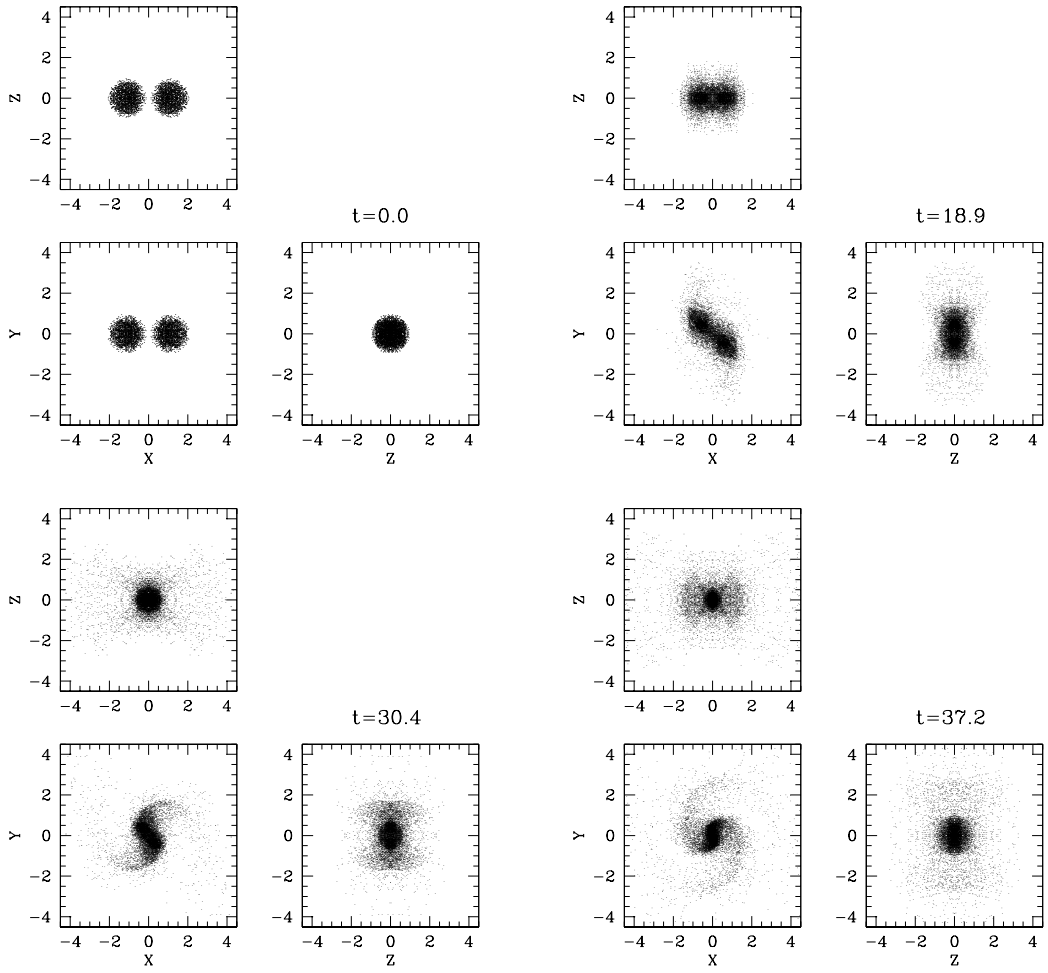

Fig. 1. (continued)

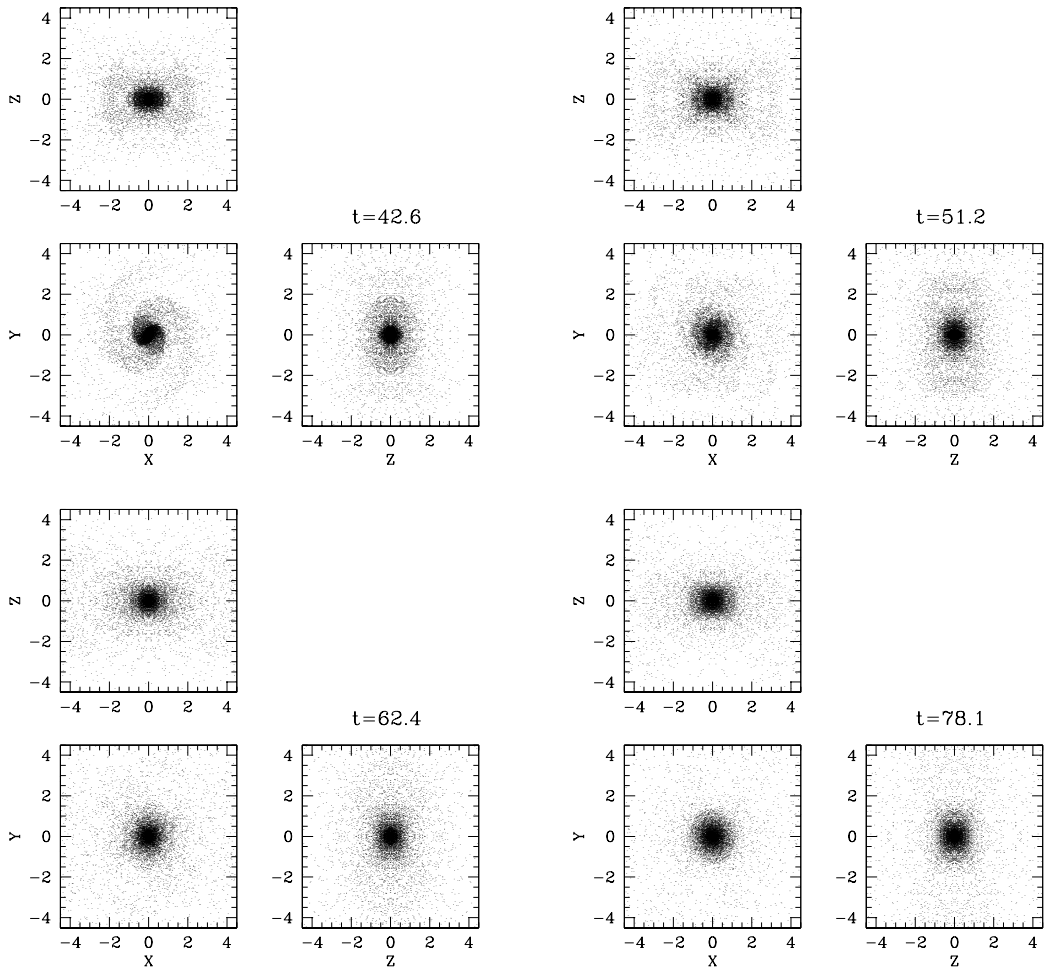

Fig. 1. Snapshots of the particle positions (denoted by dots) at selected times for a Kepler model of $M_*/r_0 = 1/6$ and $\omega_0 = 1$. Only 5×10^3 out of 10^5 are plotted. The positions are shown in units of r_0, and are projected onto $x-y$, $y-z$ and $z-x$ planes, respectively. Particles in $y < 0$ and $z < 0$ are plotted using symmetric relations assumed in this paper.

5.2.1. Products of the merger

In Figs. 1–3, we show snapshots of the particle positions at selected times for Kepler models with $M_*/r_0 = 1/6$, $1/4$ and $1/3$, respectively. (We list several characteristic quantities of the initial conditions in Table I.) In the first two cases, the final configuration consists of a new nearly axisymmetric, rotating cluster, while in the third case a black hole appears to have formed. In the last case, the simulation could not be continued until we determined the apparent horizon because the accuracy became insufficient. However, we presume that a black hole was formed, because the merged object was very compact and α and ϕ became, respectively, small (~ 0.1) and large (~ 0.7) when the simulation was terminated. The reason that we had to terminate the simulation before we determined the apparent horizon is probably

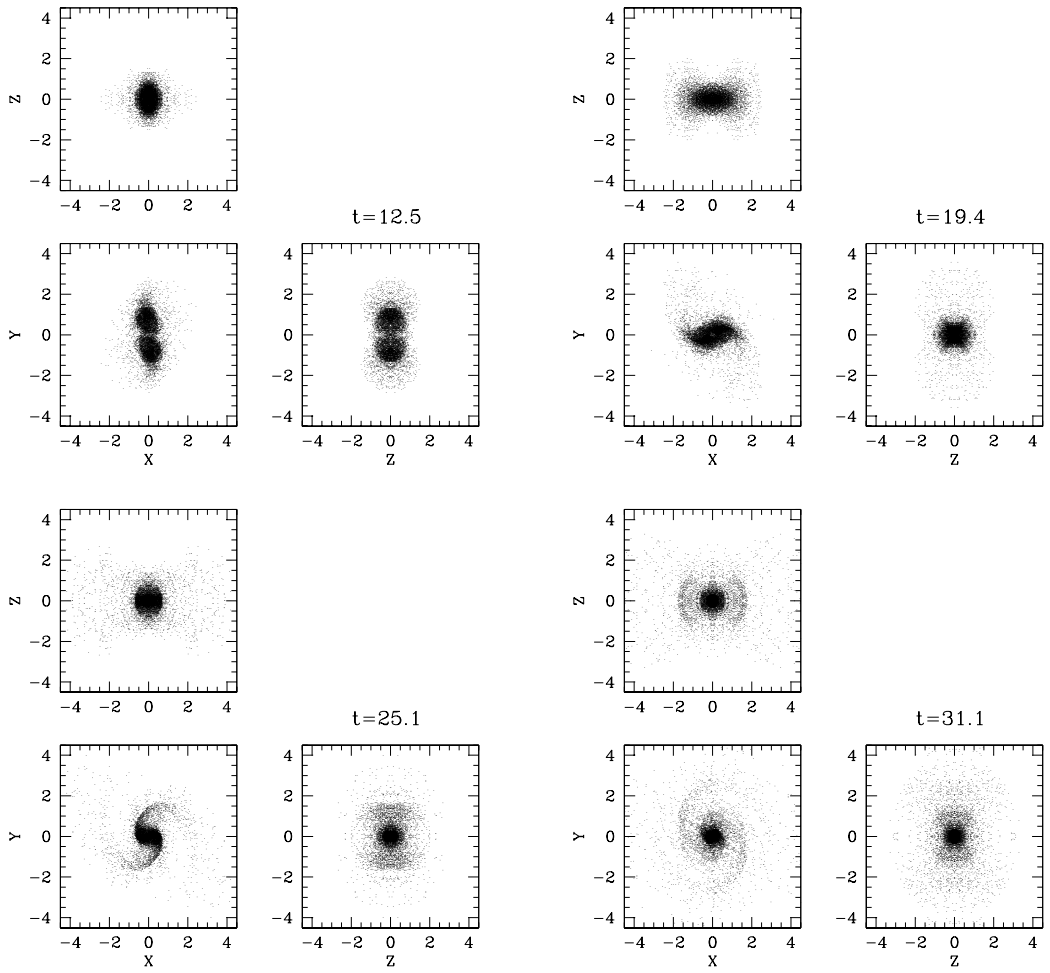

Fig. 2. (continued)

related to our AMD gauge, which seems inappropriate when applied to a problem in which black hole formation proceeds and the forming region is not well resolved. We discuss this point further below.

For the cases in which $M_*/r_0 = 1/6$ and $1/4$, we stopped our simulations at $t \sim 85 r_0$ when the new cluster seems to settle down to a nearly equilibrium state. For $M_*/r_0 = 1/6$, the core within $r < 2r_0$ in the final state comprises about 82% of the total rest mass (i.e., $m_*(2r_0)/M_* \simeq 0.82$) and about 48% of the initial total angular momentum (i.e., $j(2r_0)/J \simeq 0.48$). For $M_*/r_0 = 1/4$, we have $m_*(2r_0)/M_* \simeq 0.83$ and $j(2r_0)/J \simeq 0.61$, respectively. It appears, therefore, that the final configuration consists of dense, rapidly rotating clusters surrounded by a halo. The reason that $j(2r_0)/J$ for $M_*/r_0 = 1/6$ is smaller than that for $M_*/r_0 = 1/4$ is probably related to the fact that in the first case, self-gravity is weaker, and particles of large angular momentum can easily diffuse outward.

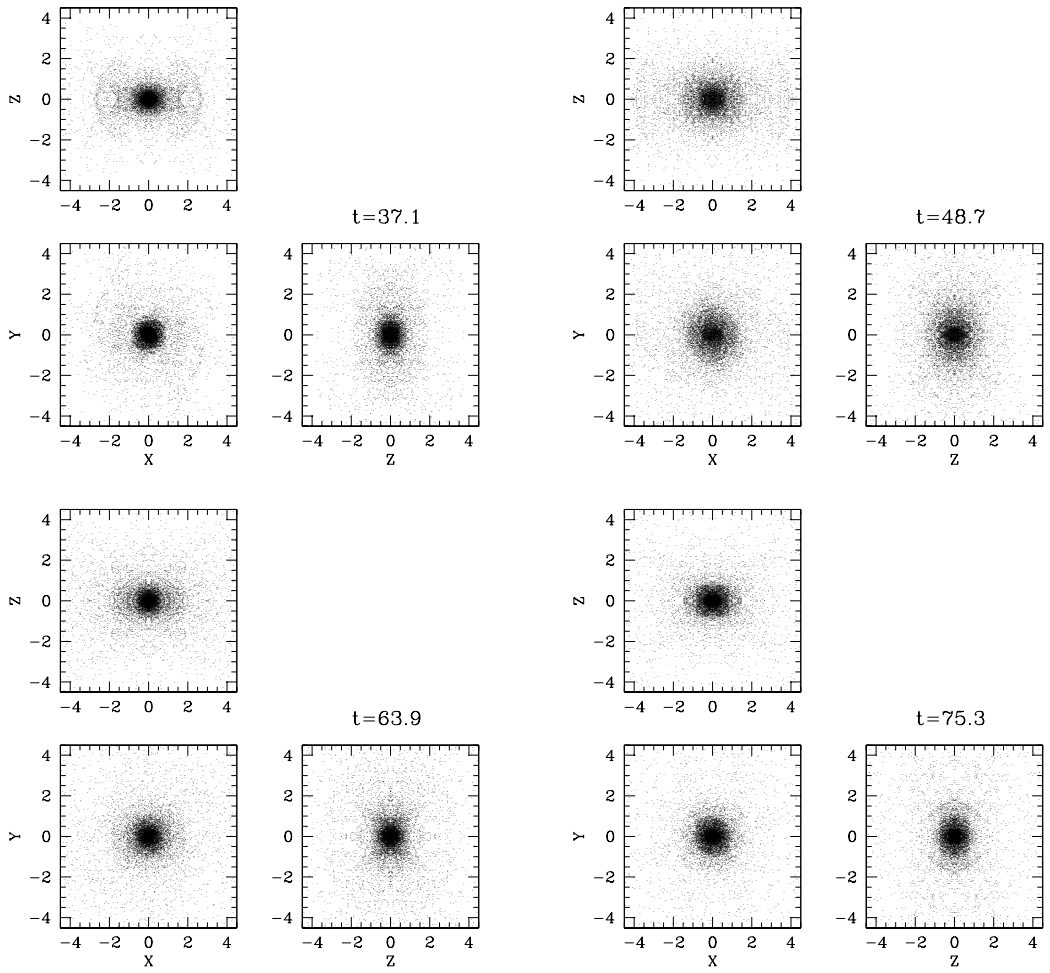

Fig. 2. The same as Fig. 1, but for Kepler model of $M_*/r_0 = 1/4$. Note that particle positions at $t = 0$ are the same as those in Fig. 1.

As shown in Figs. 1–3, the merging process toward the final state considerably depends on the initial compaction parameters. For example, for $M_*/r_0 = 1/6$, $1/4$ and $1/3$, the merging starts after about one, three quarter and half an orbital periods, respectively. Also, for $M_*/r_0 = 1/6$, the merged object initially has a triaxial ellipsoidal shape which then gradually settles down to a spheroidal object forming spiral arms and transporting the angular momentum outward. On the other hand, for $M_*/r_0 = 1/4$ and $1/3$, the merging proceeds more quickly and violently, forming a very high density object or a black hole around the mass center.

Since we did not prepare a quasi-equilibrium configuration as initial conditions for the mergers, it is difficult to present a rigorous interpretation of the results. However, we believe that the different types of behavior at the initial stages of the merger can be related to one of the three following factors. (*a*) In all cases, each cluster in a binary is tidally elongated along the axis which connects the two cluster centers just

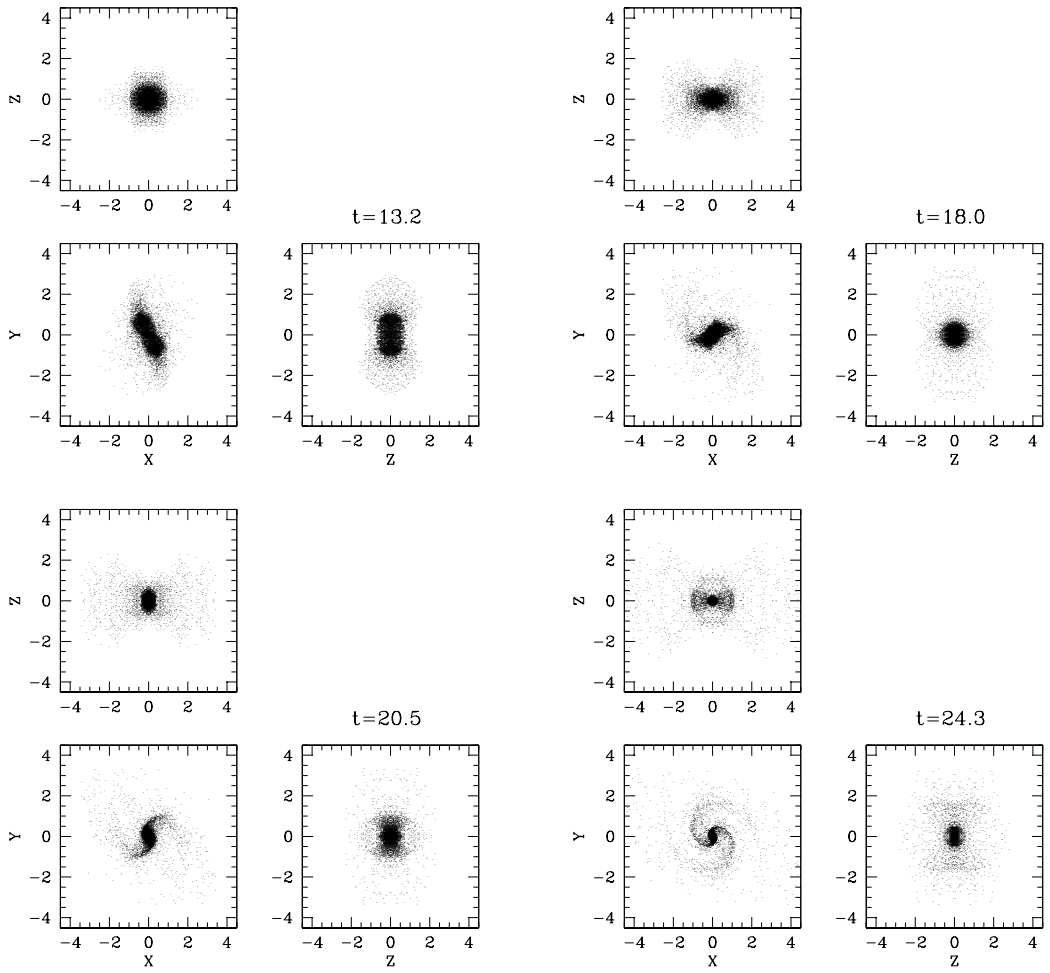

Fig. 3. The same as Fig. 1, but for Kepler model of $M_*/r_0 = 1/3$. Note that particle positions at $t = 0$ are the same as those in Fig. 1.

after the simulation starts. As a result of the elongation, each cluster in the binary acquires a quadrupole moment, which makes the attractive force between the two clusters stronger and can trigger the merging. Since the elongation may be larger for binaries of larger compaction due to a general relativistic effect, the attractive force becomes stronger for clusters of larger initial compaction. (*b*) Gravitational radiation reaction, which accelerates the merging, should be stronger for more compact binaries. This can be clearly deduced from the ratio of the coalescence time to the orbital period, which can be approximately written as [19)]

$$R_\tau \equiv \frac{5}{128\pi}\left(\frac{2r_c}{M_*}\right)^{5/2}. \qquad (5\cdot14)$$

R_τ is ~ 1.4 for $M_*/r_0 = 1/3$, while it is ~ 8 for $M_*/r_0 = 1/6$. Thus, gravitational

radiation can affect the evolution of the compact binary more efficiently. (c) For $M_*/r_0 = 1/3$ and $1/4$, the ratio of the initial orbital radius to the gravitational mass M is ~ 7 and 9, respectively, so that the orbital radius may be as small as the radius of the inner most stable orbit of the system. This implies that, for $M_*/r_0 = 1/3$ and $1/4$, a rapid transition from a stable near-circular orbit to a plunging orbit probably takes place when the orbital radius slightly decreases. On the other hand,

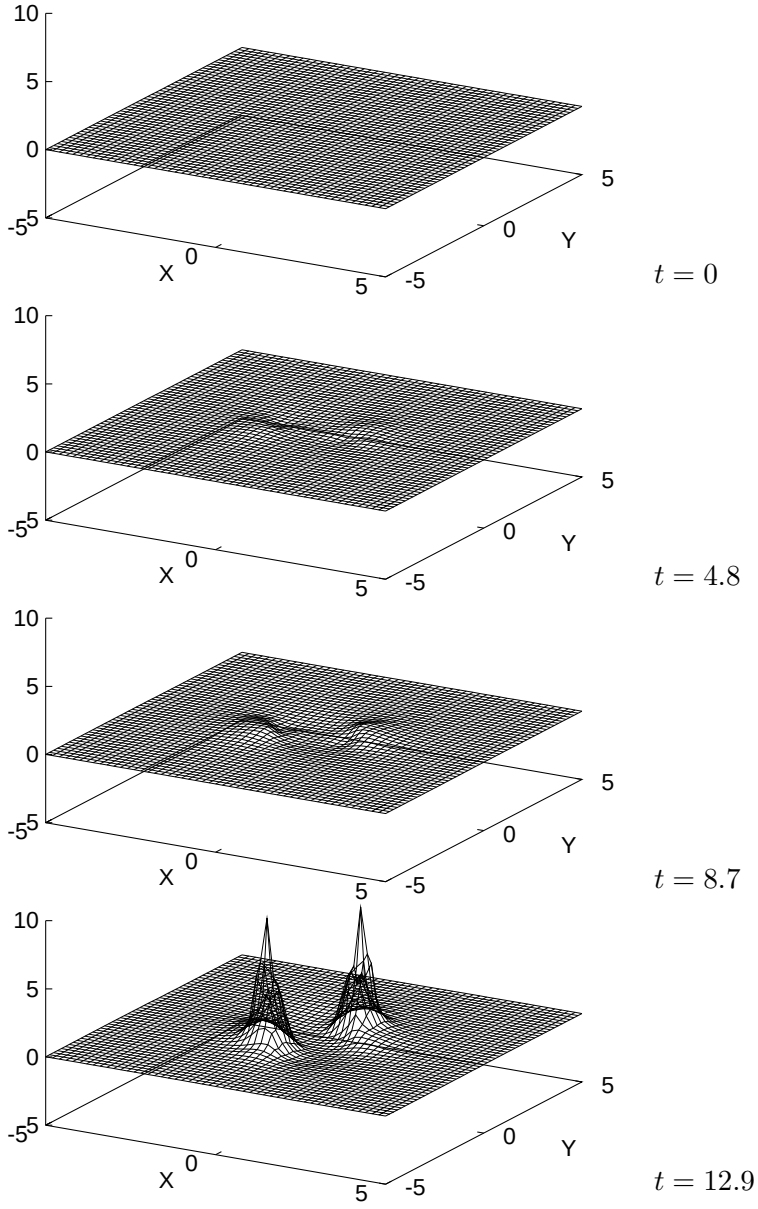

(a)

Fig. 4. (continued)

for $M_*/r_0 = 1/6$, this is never the case.

Note that all the above factors are general relativistic. Therefore, although we cannot make a firm statement on the origin of the different types of behavior for different initial compaction, it is almost certain that a general relativistic effect, which is never observed in Newtonian simulations, is crucial in these simulations.

The evolution in the late phase of the merger is also different for the three models.

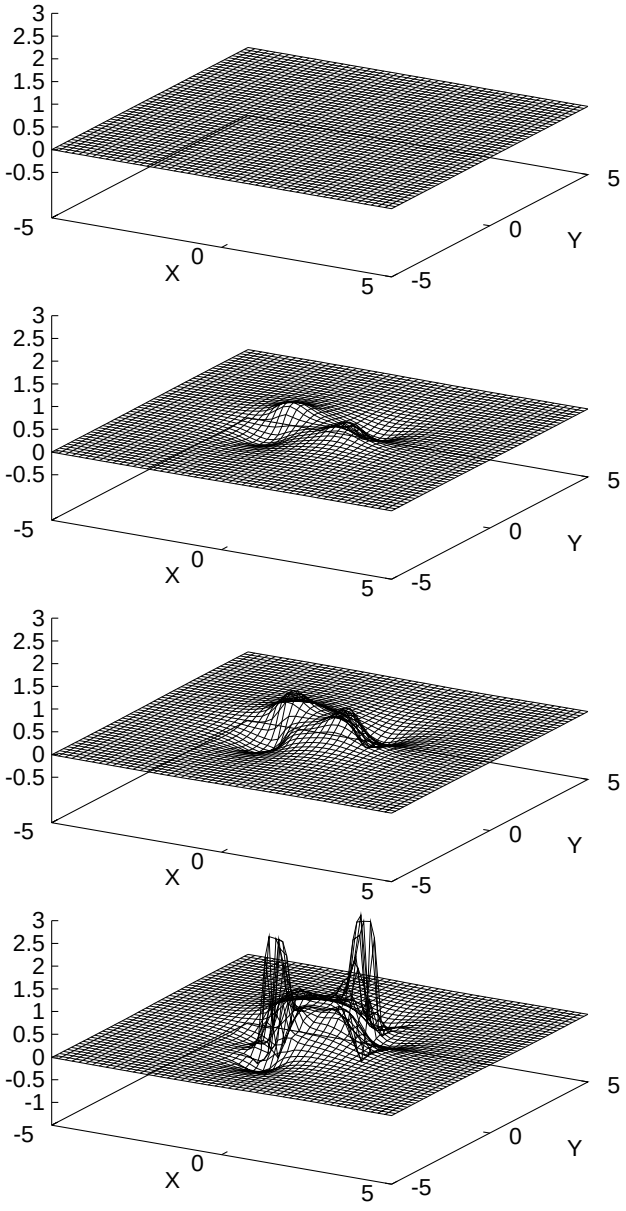

(b)

Fig. 4. (continued)

In particular, for $M_*/r_0 = 1/4$, we find an interesting feature which appears to be a peculiarity of the merger between collisionless clusters. In this case, the two clusters merge to form a very high density cluster in the early phase ($t \sim 30r_0$). Then, a large fraction of particles expands outward ($t \sim 30r_0 - 50r_0$), and the central density decreases. Because the system is strongly bound, the particles eventually converge in the central region ($t > 50r_0$) to produce a final compact cluster. A possible

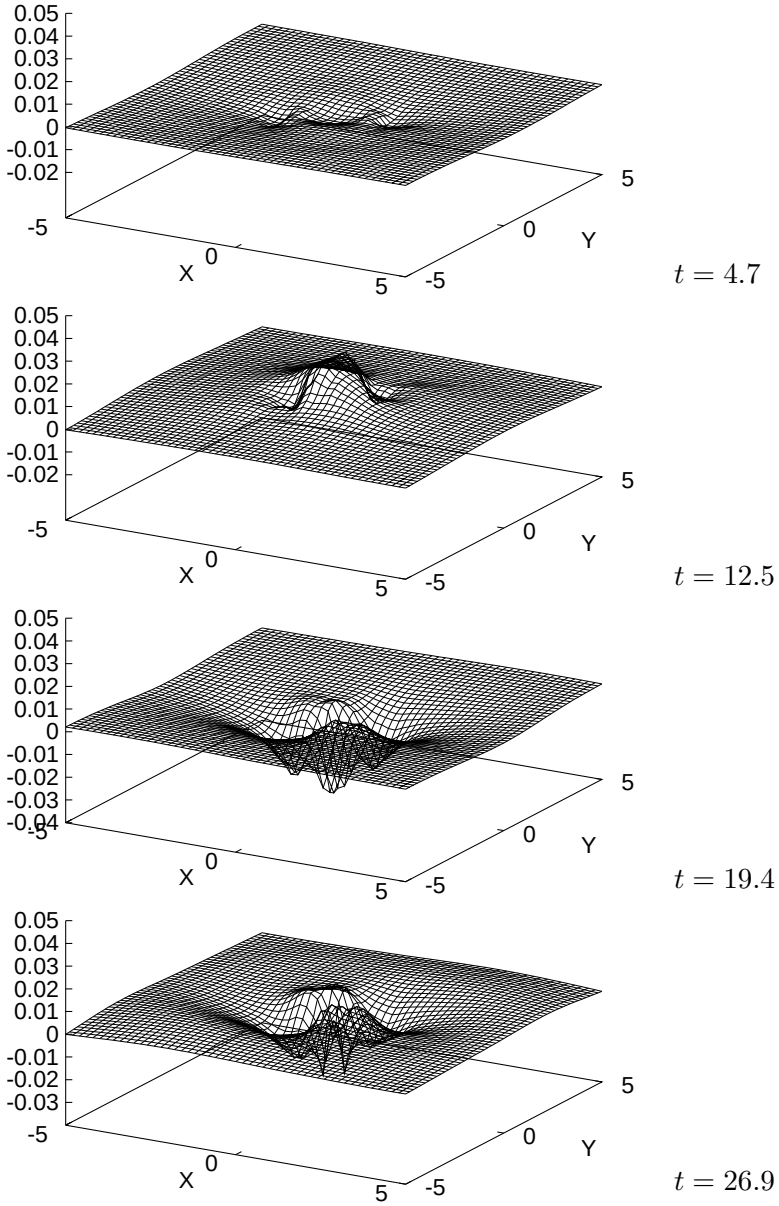

(c)

Fig. 4. (continued)

explanation for the outward motion for $t \sim 30 - 50 r_0$ can be found in the peculiar nature of a collisionless system, which does not possess any efficient mechanism of conversion of the kinetic energy into internal energy. In contrast, in the merger between fluid stars, a shock is formed, and the kinetic energy may be converted to the thermal energy. Consequently, most of the mass (or energy) in the system may

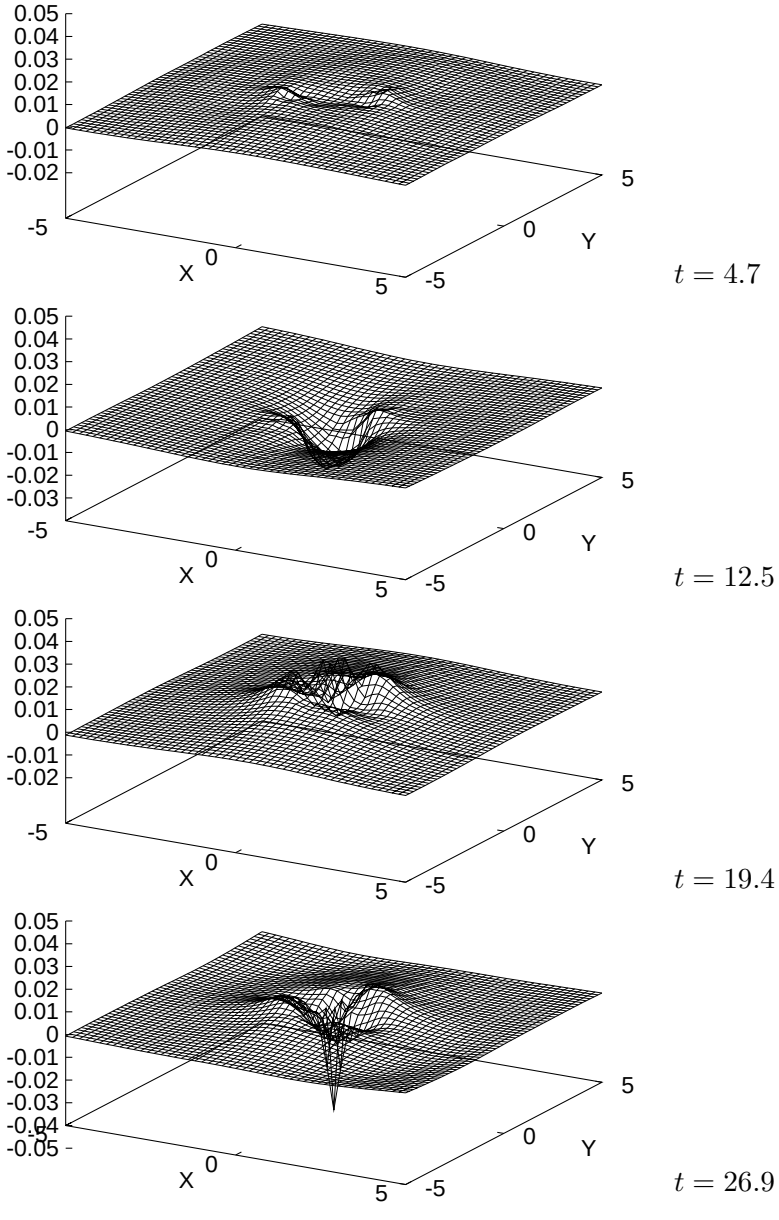

(d)

Fig. 4. h_{xx}((a) and (c)) and h_{yy} ((b) and (d)) in the equatorial plane at selected times for $\beta^k = 0$ gauge((a) and (b), and for AMD gauge ((c) and (d)). Note that the scaling of the height is considerably different between Figs. 4(a), (b) and (c), (d) (see text).

be trapped near the mass center.

For $M_*/r_0 = 1/4$, we have also performed a simulation using the zero shift gauge condition ($\beta^k = 0$). In this case, the large coordinate distortion leads to increasing large values of $\tilde{\gamma}_{ij}$ and produces very inaccurate results in a time $\sim 1/3$ orbital period. We show h_{xx} and h_{yy} in the equatorial plane for $\beta^k = 0$ and $M_*/r_0 = 1/4$ at selected times in Figs. 4(a) and (b), respectively. It is found that the maximum (minimum) value monotonically increases (decreases), and near $t \sim 13r_0$ it becomes ~ 9 (-0.5) for h_{xx} and ~ 2.4 (-0.5) for h_{yy}. In contrast, in the simulations with our AMD gauge, the maximum (minimum) value of h_{xx} and h_{yy} does not monotonically increase (decrease) (see Figs. 4 (c) and (d)). Since we start the simulation with a conformal flat initial condition, it initially increases or decreases monotonically, but the maximum (minimum) stops increasing (decreasing) in about one orbital period when they have reached $\sim \pm 0.05$. This behavior is a clear indication that the AMD gauge condition provides the required suppression of the coordinate distortion.

Note that the magnitudes of h_{ij} are roughly consistent with h_{ij} being a second post-Newtonian quantity, i.e., of $O[(M_*/r_0)^2]$. This confirms that our AMD gauge condition is actually a valid approximation of the MD gauge conditions, because the coupling terms between h_{ij} and β^k are sufficiently small. Since h_{ij} does not monotonically increase nor decrease and the absolute value of each component remains small, simulations can be stably and accurately performed for a time much longer than the dynamical time scale using our AMD gauge condition.

In Figs. 5 and 6, we show snapshots of the particle positions at selected times for corotating models of $M_*/r_0 = 1/4$ and $1/3$. These figures should be compared with Figs. 2 and 3, respectively. As in the Kepler case, the final product of the less compact binary is a rotating cluster, while that of the more compact binary appears to be a black hole. In the case $M_*/r_0 = 1/3$, again the simulation could not be continued until the apparent horizon was determined.

By comparing Figs. 2 and 5, we find that the merging process in corotating models is different from that occurring in Kepler models, and this is particularly evident for the case $M_*/r_0 = 1/4$. In general, in the cases of corotating initial conditions, the outer part of the binary has more angular momentum than that for the Kepler model, so that the centrifugal force is stronger. Hence, the merging proceeds mainly in the inner region of the system, and particles in the outer region are not involved. Since the two clusters do not collide very quickly and the merging proceeds gradually, the resulting object does not expand outward significantly after the merger when compared with the Kepler case. The product of the merger settles down to a spheroidal object more gradually, forming spiral arms in the outer region. In this case, $m_*(2r_0)/M_* \simeq 0.79$ and $j(2r_0)/J \simeq 0.48$ in the final stage at which we terminated computation, i.e., at $t \sim 80r_0$. The fact that the final value of $j(2r_0)/J$ is smaller than that for the Kepler model with the same initial compaction results from the initial corotating velocity field, in which the outer parts have a large angular momentum and are therefore able to diffuse outward more easily.

In order to clarify the reason that both our AMD gauge and the MD gauge conditions are not well suited to study the formation of a black hole, we also performed simulations for a Kepler model of $\omega_0 = 0.5$ with $M_*/r_0 = 1/3$. In this case, the an-

gular momentum is not large enough to counteract the gravitational force between the two clusters, and they quickly merge into a black hole. In this simulation, we set $N = 50000$, and the grid spacing was $\delta x = r_0/15$.

As in the Kepler and corotating cases with $\omega_0 = 1$ and $M_*/r_0 = 1/3$, the simulation using the AMD gauge condition terminated before an apparent horizon was formed. The reason for this seems to be the following: Using a MD gauge condition or our AMD gauge condition with $K = 0$, Eq. (3·7) can be roughly approximated as

$$\Delta\beta^i{}_{,i} \sim 12\pi J_{i,i} \quad . \tag{5·15}$$

During a gravitational collapse we have

$$J_r < 0, \text{ and } J_{i,i} \sim \frac{1}{r^2}\partial_r(J_r r^2) < 0, \tag{5·16}$$

where J_r denotes the radial component of J_i and we assume that the matter collapses

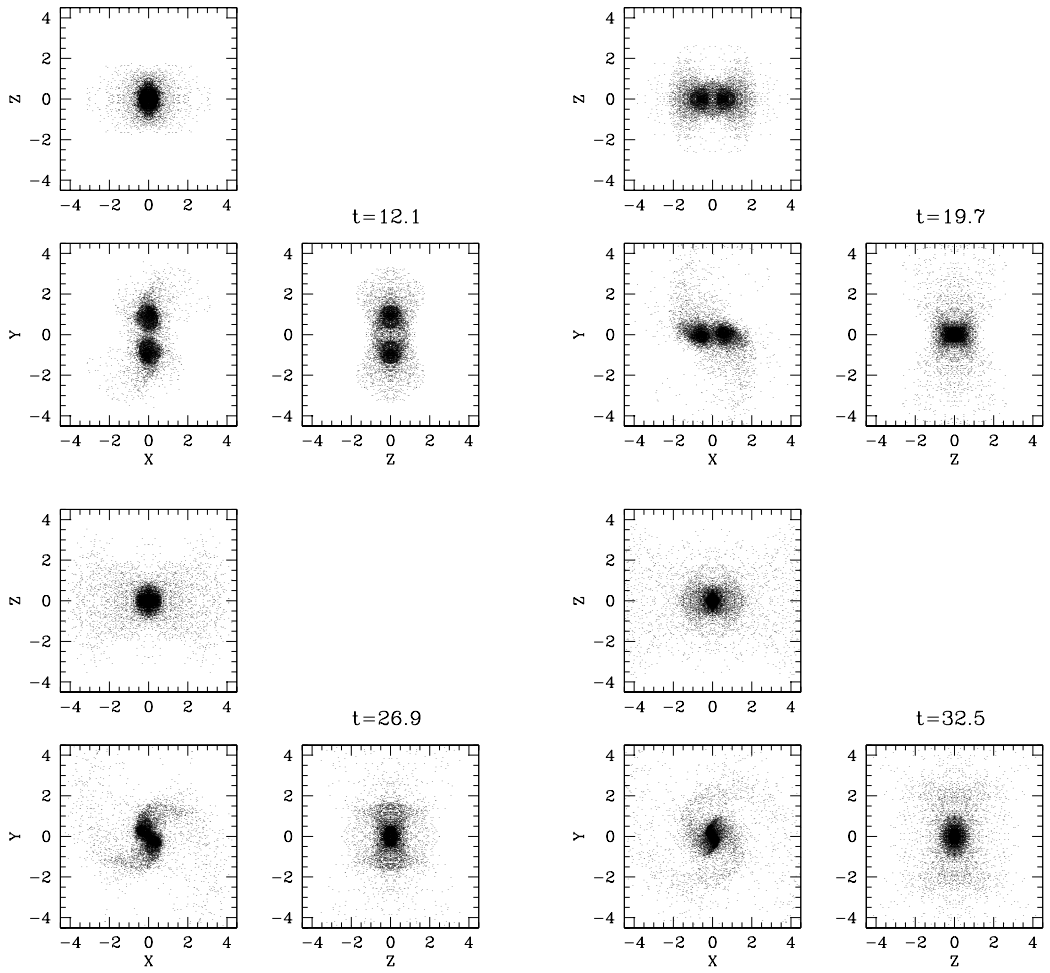

Fig. 5. (continued)

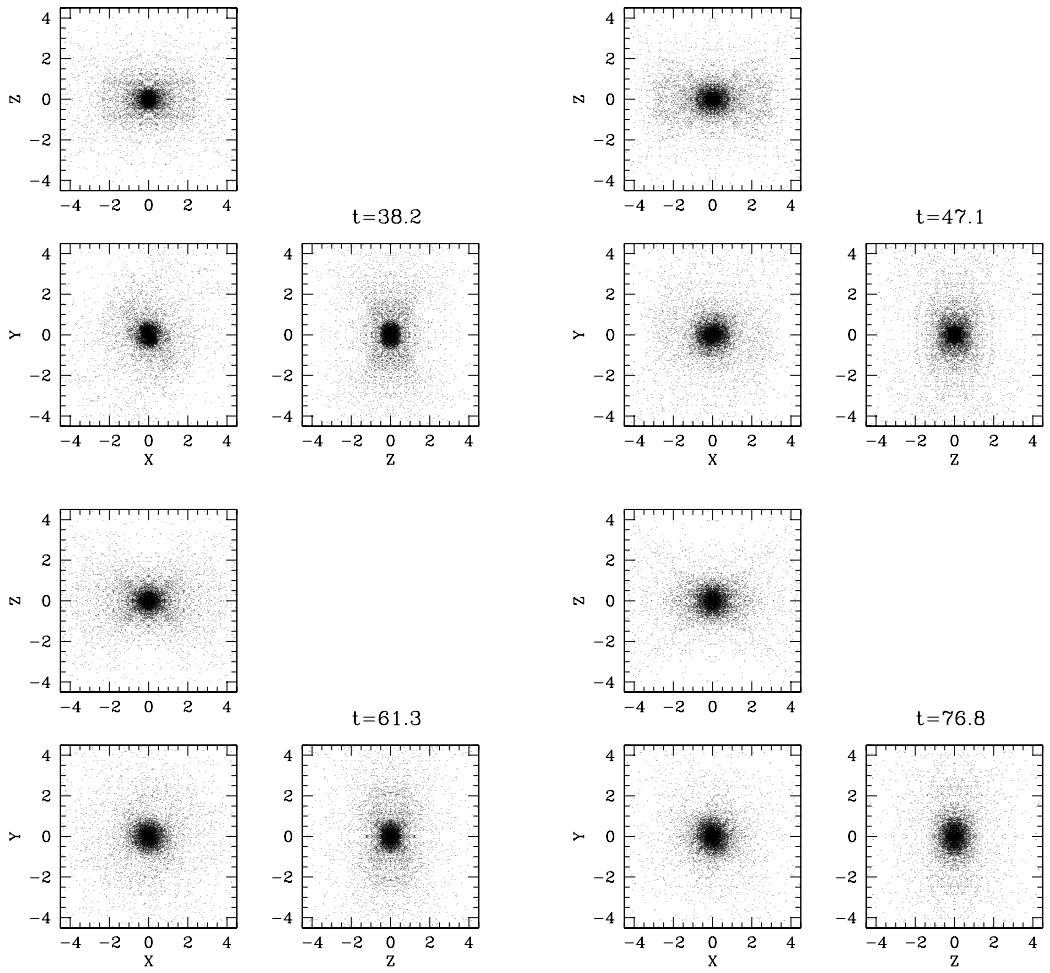

Fig. 5. The same as Fig. 1, but for a corotating model of $M_*/r_0 = 1/4$. Note that particle positions at $t = 0$ are the same as those in Fig. 1.

mainly in the radial direction. Thus, in the central region where the black hole formation takes place, the divergence of β^i is positive, i.e.,

$$\beta^i{}_{,i} > 0 \text{ and } \beta^r > 0. \tag{5·17}$$

Clearly, the condition $\beta^r > 0$ implies that coordinates spread radially outward; i.e., the physical size between two neighboring grids increases and the numerical resolution deteriorates.[20] At $r = 0$, ϕ increases rapidly when the collapse begins (see the solid line in Fig. 7); for $t \sim 14r_0$, $\phi \sim 0.8$ while it was ~ 0.13 at $t = 0$. As a result of this variation in ϕ, the physical separation between two neighboring grid points around $r = 0$ increases by a factor of $e^{1.4} \sim 4$. If we require the same accuracy as that at $t = 0$, we have to reduce the grid spacing δx by a factor of 4, which is not feasible in a 3D numerical simulation. This problem might be resolved with the help of an adaptive mesh refinement (AMR) technique.[21] However, ϕ increases more and

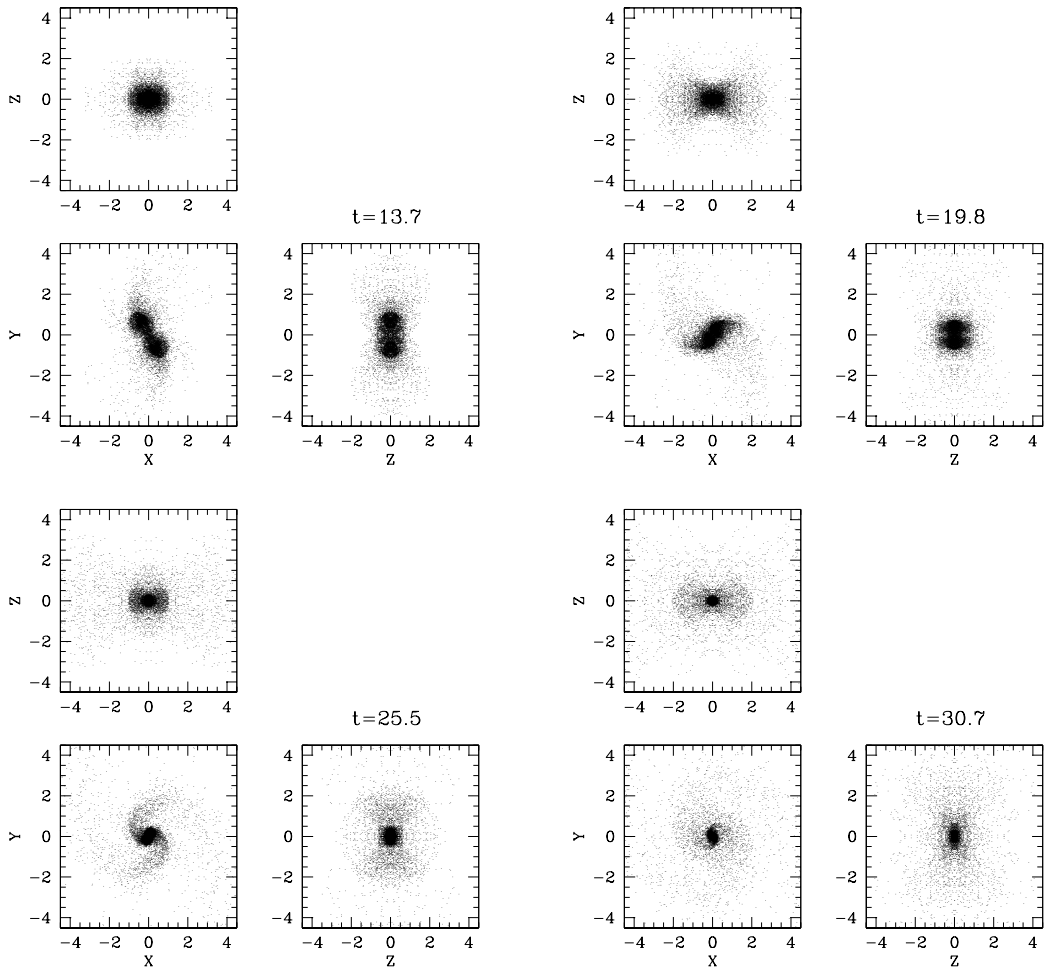

Fig. 6. The same as Fig. 1, but for a corotating model of $M_*/r_0 = 1/3$. Note that particle positions at $t = 0$ are the same as those in Fig. 1.

more as the collapse proceeds, so that even an AMR treatment might be insufficient without changing the gauge condition once a gravitational collapse begins. In this paper, thus, we propose a modified spatial gauge condition derived from our AMD condition as

$$\beta^k = \beta^k_{\rm AMD} - \frac{x^k}{r+\epsilon}\beta^{r'}_{\rm AMD} f(r,t), \tag{5·18}$$

where $\beta^k_{\rm AMD}$ is the shift vector determined from our AMD gauge condition, $\beta^{r'}_{\rm AMD} = x^k\beta^k_{\rm AMD}/(r+\epsilon)$, ϵ is a small constant and $f(r,t)$ is a function of r which satisfies $f(r=0) = O(1)$ and $f(r=\infty) = 0$. In this case, β^r around a black hole forming region can be set to a small value. Although the distortion in $\tilde{\gamma}_{ij}$ due to the radial motion increases, the coordinate twisting due to the angular motion may still be suppressed. Furthermore, the TT property is preserved in the wave zone because $f(r,t) \to 0$ for $r \to \infty$. To validate this idea, we perform a simulation using the

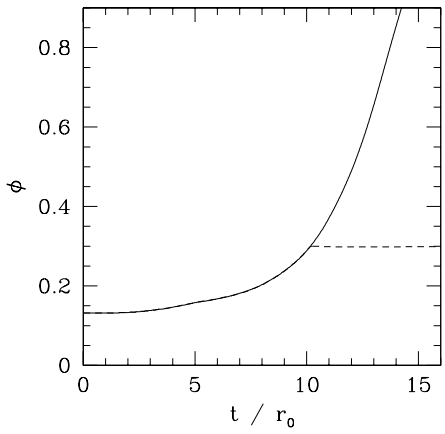

Fig. 7. ϕ at $r = 0$ as a function of t for a Kepler model of $M_*/r_0 = 1/3$ and $\omega_0 = 0.5$ with AMD gauge of $f_0 = 0$ (solid line), and non-zero f_0 case (dashed line), respectively.

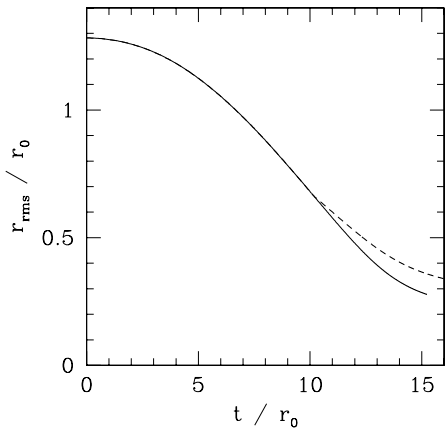

Fig. 8. $r_{\rm rms}/r_0$ as a function of t for a Kepler model of $M_*/r_0 = 1/3$ and $\omega_0 = 0.5$ with AMD gauge of $f_0 = 0$ (solid line), and non-zero f_0 case (dashed line), respectively.

following $f(r,t)$ as an example,

$$f(r,t) = f_0(t)\frac{1}{1+(r/3M_*)^6}, \tag{5·19}$$

where we choose f_0 to be

$$f_0(t) = \begin{cases} 1 & \text{for } \alpha(r=0) \le 0.5, \\ 0 & \text{for } \alpha(r=0) > 0.5. \end{cases} \tag{5·20}$$

In Fig. 7, we show ϕ at $r = 0$ for f_0 of Eq. (5·20) (the dashed line) as well as for $f_0 = 0$ (the solid line). The behavior of ϕ clearly shows that the coordinate spreading is suppressed after we turn on a non-zero f_0. In Fig. 8, we also show the root mean square of the coordinate position for particles defined as

$$r_{\rm rms} \equiv \sqrt{\frac{1}{N}\sum_{i,a} x_a^i x_a^i}. \tag{5·21}$$

Although the physical results of these simulations should be identical, the time evolution of $r_{\rm rms}$ in each simulation should be different when different gauge conditions are adopted. Since the coordinate position of each particle becomes smaller when the radial coordinate spreads outward, we expect $r_{\rm rms}$ to be smaller for a smaller f_0. Figure 8 clearly reflects this property and that the non-zero f_0 suppresses the coordinate spreading effect.

In Figs. 9 and 10, we also show snapshots of particle positions at selected times for $f_0 = 0$ and the non-zero f_0, respectively. We find that in the $f_0 = 0$ case and at late time, particles are concentrated in very narrow regions around the origin and, as a consequence, the resolution becomes insufficient for $t \sim 14r_0$. On the other

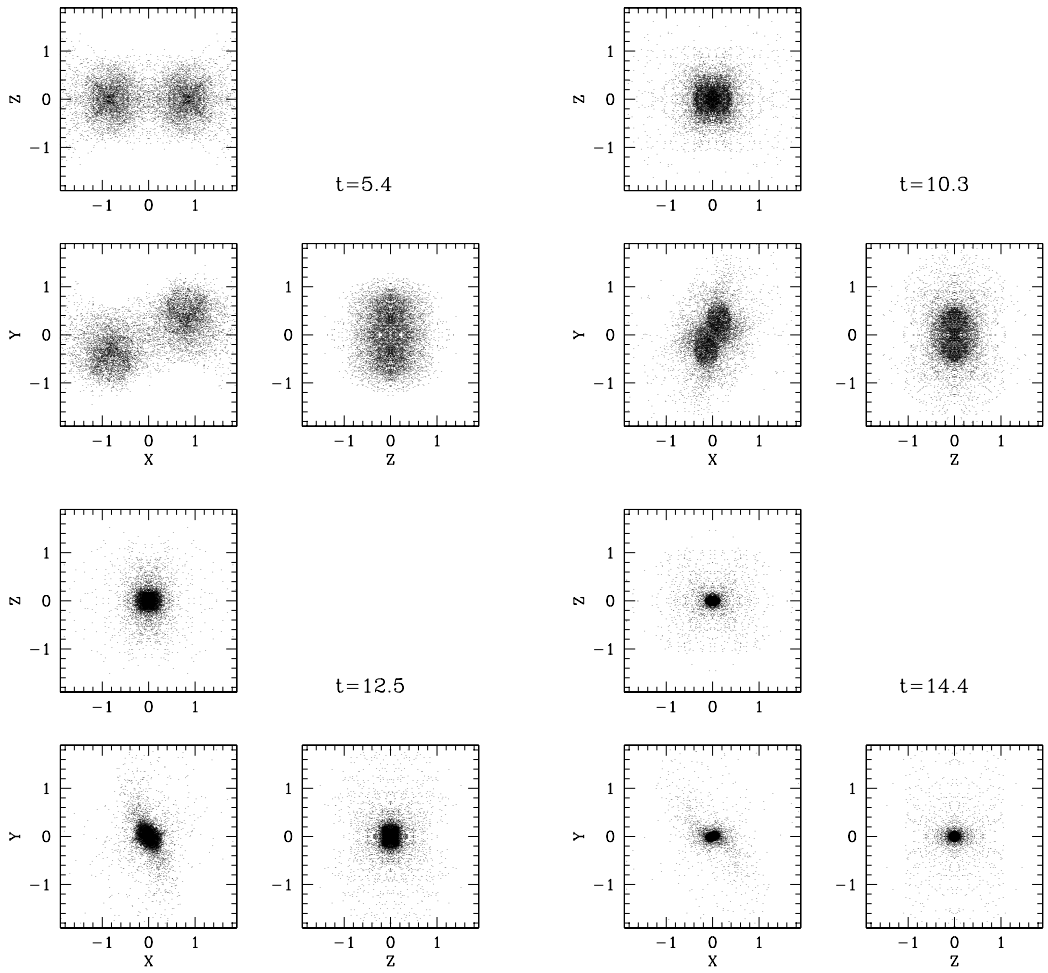

Fig. 9. The same as Fig. 3, but for Kepler model of $\omega_0 = 0.5$.

hand, in the non-zero f_0 case, the coordinate spreading was not appreciable, at least up to the formation of an apparent horizon, and the simulation continued after the formation of the apparent horizon and for a long enough time that the horizon stretching became dominant and spoiled the numerical accuracy. In conclusion, we can mention that in addition to our AMD gauge condition, it may be helpful to incorporate an appropriate non-zero function $f(r,t)$ in the final phase of the merger just before the formation of a black hole.

It is important to stress that the present strategy to compensate for the limitation of MD-type gauge conditions is well suited to the problem under investigation and is not the only possible solution. In a different scenario, different solutions might turn out to be more effective. Consider, for example, the case in which a rapidly rotating object collapses and a disk is formed prior to the formation of a black hole. In this case, it would probably be more appropriate to suppress β^z first, and then,

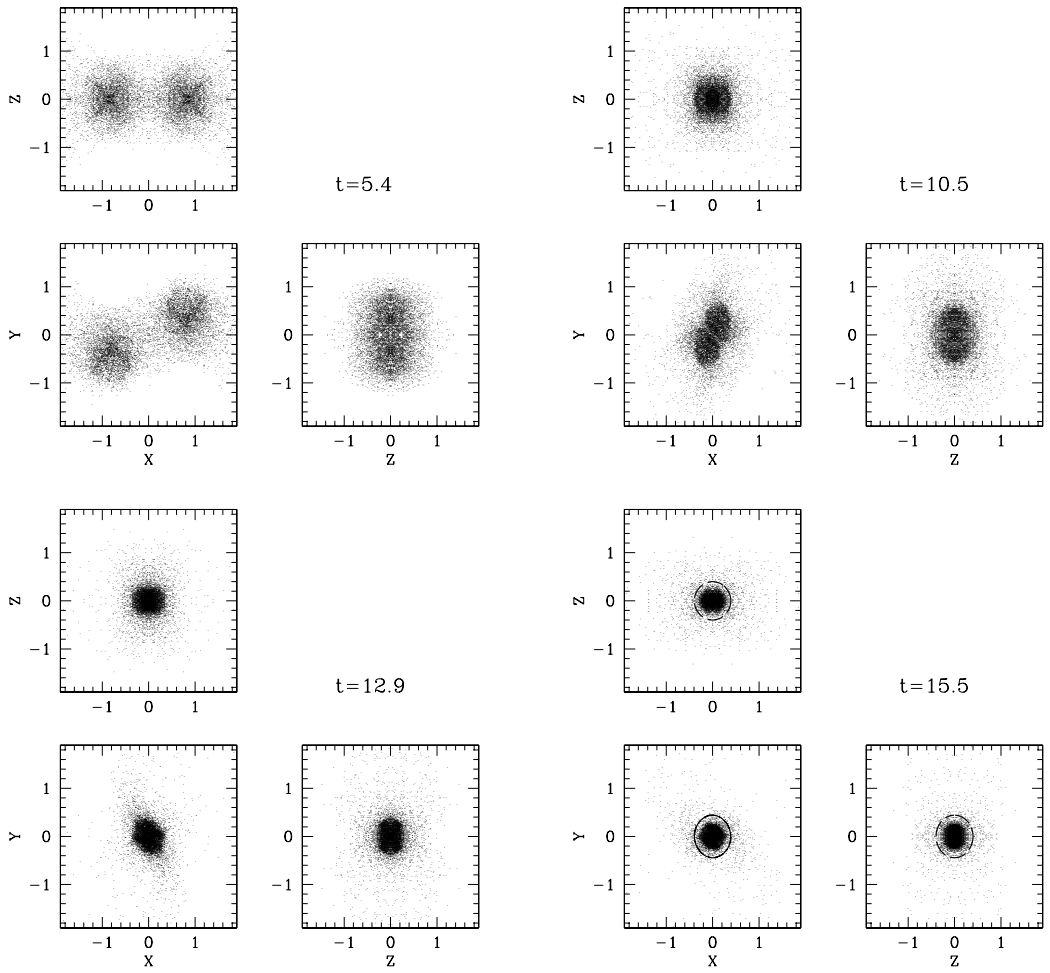

Fig. 10. The same as Fig. 9, but in a modified gauge condition with non-zero f_0. The dashed lines at $t = 15.5r_0$ and $r \sim 0.5r_0$ denote locations of the apparent horizon in x-y, z-y and x-z planes, respectively.

$\beta^R[\equiv (x\beta^x + y\beta^y)/\sqrt{x^2+y^2}]$ only when the black hole formation starts. It is evident that more detailed studies on the choice of the gauge condition suitable to study the formation of a black hole are necessary.

5.2.2. Gravitational waveforms

In Figs. 11 and 12, we show $h_+/(M_*^2/r_0)$ and $h_\times/(M_*^2/r_0)$ at $z_{\rm obs} = 7.5r_0$ (solid lines) and $6r_0$ (dashed lines) for the Kepler and corotating models with $M_* = r_0/4$, respectively. We plot these lines as a function of $(t - z_{\rm obs})/r_0$. Hence, if h_+ and $h_\times$ behave as solutions of the wave equations near the outer boundaries, the two lines should approximately agree. Note that gravitational waves begin to reach the observer at $t - z_{\rm obs} \simeq 0$, so that the waveforms shown for $t - z_{\rm obs} < 0$ are meaningless as the coalescence waveforms.

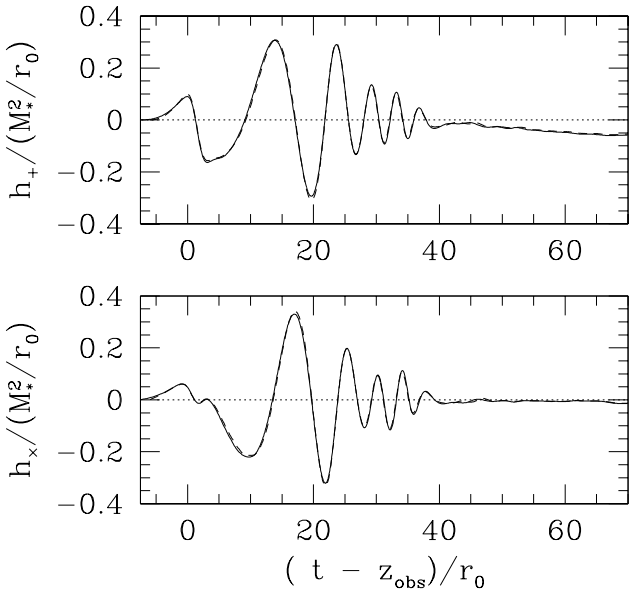

Fig. 11. h_+ and $h_\times$ at $z_{\rm obs} = 7.5r_0$ (solid line) and $z_{\rm obs} = 7.5r_0$ (dashed line) as a function of $(t - z_{\rm obs}/r_0)$ for a Kepler model of $M_*/r_0 = 1/4$ and $\omega_0 = 1$.

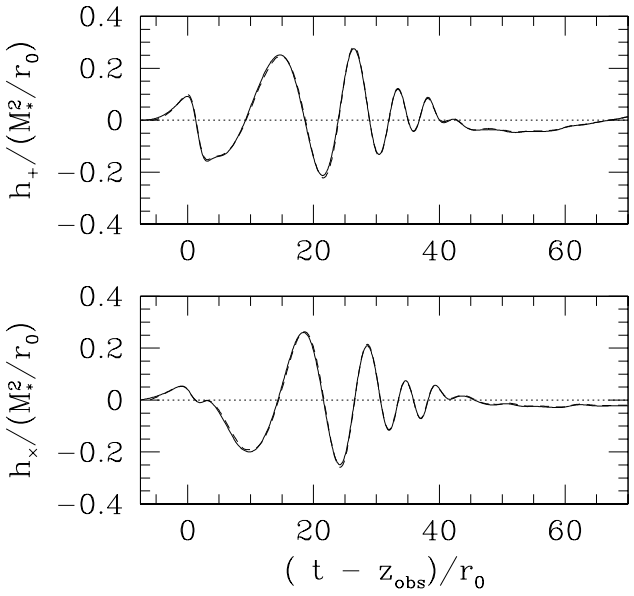

Fig. 12. The same as Fig. 11, but for a corotating model of $M_*/r_0 = 1/4$.

It should be mentioned that the expected wavelength of gravitational waves in the initial phase of the merger is approximately $T/2 \simeq 20r_0$, where T is an approximate orbital period (see Table I for definition of T). In principle, the asymptotic waveforms should be extracted in the wave zone, and therefore for $z_{\rm obs} > 20r_0$. Nevertheless, the waveforms shown here appear to constitute a fair description of the asymptotic waveforms due to the following reasons: (*i*) The solid and dashed lines agree well in both cases throughout the computations, so that h_+ and $h_\times$ actually propagate at the speed of light. (*ii*) The wavelength in the initial phase of the merger approximately agrees with that expected from the initial orbital period. (*iii*) The amplitude of h_+ and $h_\times$ in the initial phase roughly agrees with an analytical estimate using the quadrupole formula for two-point masses in a circular orbit, i.e., $M_*(4\pi r_c/T)^2 = M_*^2/2r_c$.[19] (*iv*) The waveforms agree fairly well with those expected from Figs. 2 and 5; i.e, in their initial merging phases, the amplitudes of gravitational waves are the largest because the systems are highly non-axisymmetric, but once they settle down to form an elliptical merged object, the amplitude gradually decreases.

The gravitational waveforms in Figs. 11 and 12 also reflect the difference in the merger process for the Kepler and the corotating models. In the Kepler case, the merging quickly proceeds to form a new, high density rotating object resulting in a rapid and large increase in the amplitude of gravitational waves. In the corotating model, on the other hand, the merging proceeds less rapidly, and the resulting amplitude of gravitational waves is smaller. Also, in the Kepler case, a high density and rapidly rotating ellipsoidal object is formed after the merger, and it is responsible for the emission of high frequency gravitational waves. The results presented here suggest that waveforms of gravitational waves from the merger of stellar clusters may be sensitive to the internal velocity fields that two clusters possess before the merger, and could be used to extract astrophysical information.

In both the Kepler and the corotating cases, the maximum values of h_+ and $h_\times$ are roughly $\sim 0.08M_*(4M_*/r_0)$ and the wavelength is $\sim 10r_0(r_0/4M_*)^{1/2}$, as expected from the quadrupole formula. If similar mergers between highly relativistic clusters actually occurred in the early universe, the amplitude of gravitational waves could be

$$\sim 10^{-18}\left(\frac{4000\,\mathrm{Mpc}}{r}\right)\left(\frac{M_*}{10^6\,M_\odot}\right)\left(\frac{4M_*}{r_0}\right), \tag{5·22}$$

with the frequency $\sim 10^{-2}(10^6\,M_\odot/M_*)(4M_*/r_0)^{3/2}$ Hz, where $M_\odot$ denotes the solar mass. If mergers between highly relativistic star clusters of mass $\sim 10^6\,M_\odot$ and radius $\sim 10M_*$ occurred in the early universe, it should be possible to detect emitted gravitational waves by the planned gravitational wave detectors in space.[6]

In Figs. 13 and 14, we show $rR_{2,2\pm}/r_0$ as a function of $(t - r_{\rm obs})/r_0$ for the Kepler and the corotating models of $M_* = r_0/4$, where we define

$$R_{2,2+} \equiv \frac{R_{2,2} + R_{2,-2}}{\sqrt{2}}, \tag{5·23}$$

$$R_{2,2-} \equiv \frac{R_{2,2} - R_{2,-2}}{\sqrt{2}i}. \tag{5·24}$$

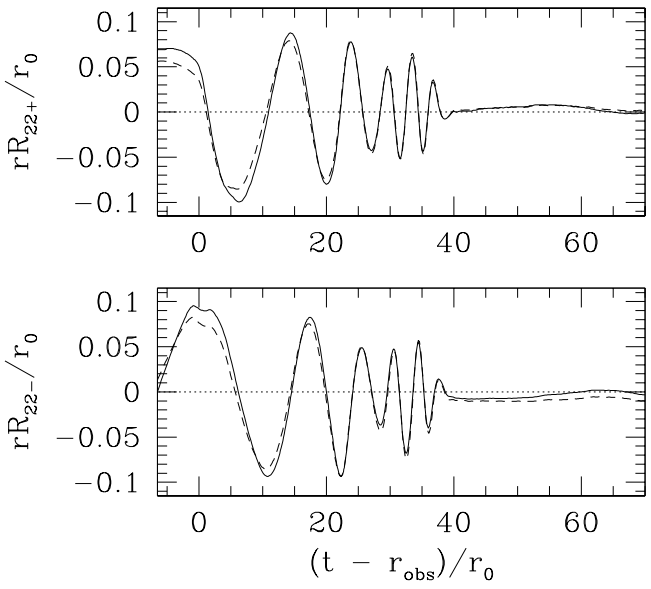

Fig. 13. rR_{22+} and rR_{22-} at $r_{\rm obs} = 6.5r_0$ (solid line) and $r_{\rm obs} = 7.3r_0$ (dashed line) as a function of $(t - r_{\rm obs})/r_0$ for a Kepler model of $M_*/r_0 = 1/4$ and $\omega_0 = 1$.

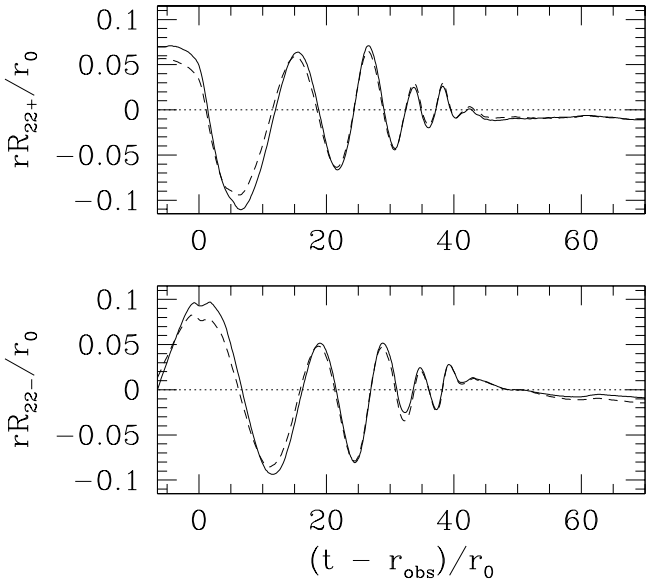

Fig. 14. The same as Fig. 13, but for a corotating model of $M_*/r_0 = 1/4$.

The solid and dashed lines denote the waveforms extracted at $r_{\rm obs} = 6.5r_0$ and $7.3r_0$, respectively.

We find that for $rR_{2,2\pm}$, the solid and dashed lines do not coincide well compared with those for h_+ and $h_\times$. In particular, for $t - r_{\rm obs} < 10r_0$, in which case the variation time scale of the system is relatively long, the coincidence is not good. The disagreement is probably due to the fact that the main contribution to $R_{2,2\pm}$ comes not only from the $O(r^{-1})$ part of $\tilde{\gamma}_{ij}$ but also from the $O(r^{-3})$ part of $\exp(\phi)$, which can be approximated for large r as

$$\exp(\phi) = 1 + \frac{M}{2r} + \frac{3\mathcal{I}_{ij}x^i x^j}{4r^5} + O(r^{-5}), \tag{5·25}$$

where $\mathcal{I}_{ij}$ denotes the trace free part of a quadrupole moment. An order of magnitude estimate for $l = |m| = 2$ modes of h_{ij} and $\exp(\phi)$ is given by

$$h_{ij} \sim \frac{1}{r}\frac{d^2\mathcal{I}_{ij}}{dt^2}, \text{ and } \exp(\phi) \sim \frac{\mathcal{I}_{ij}}{r^3}. \tag{5·26}$$

As a result, the ratio of the magnitude of h_{ij} to that of $\exp(\phi)$ is $\sim (\omega r)^2$, where ω denotes a characteristic angular frequency of gravitational waves. In order to extract gravitational waves (i.e., the contribution from h_{ij}) clearly, ωr should be much larger than unity. However, for $t - r_{\rm obs} \sim 0$, we extract $R_{2,2\pm}$ for $r \sim \omega^{-1}$, and the magnitudes of the two contributions are roughly equal. For this reason, the solid and dashed lines do not coincide well, and $R_{2,2\pm}$ for $t - r_{\rm obs} < 10r_0$ should not be regarded as accurate quantities for measuring gravitational waves.

However, when ω is sufficiently large, the coincidence between the solid and dashed lines is improved, and for $t - r_{\rm obs} \sim 10 - 40r_0$, the coincidence is fairly good. Assuming the quantities $R_{2,2\pm}$ describe gravitational waveforms correctly, we can calculate the total energy luminosity ΔE due to $l = |m| = 2$ components by integrating dE/dt from $t - r_{\rm obs} = 10r_0$ to the end of the simulations using Eq. (4·10). We obtain for the Kepler and corotating models, respectively,

$$\Delta E \simeq 4.5 \times 10^{-3} M_* \text{ and } 1.5 \times 10^{-3} M_*. \tag{5·27}$$

For a binary composed of equal masses in a circular orbit of orbital radius $2r_c$, the energy radiated by gravitational waves in one orbital period is roughly given by the quadrupole formula as [19]

$$\Delta E \sim \frac{4\pi}{5}\left(\frac{M_*}{2r_c}\right)^{7/2} M_* = 1.24 \times 10^{-3} M_* \left(\frac{4M_*}{r_0}\right)^{7/2} \left(\frac{1.1r_0}{r_c}\right)^{7/2}, \tag{5·28}$$

which confirms the validity of the results obtained in Eq. (5·27). The reason that ΔE for the Kepler model is larger than that for the corotating model is that the merging proceeds more quickly and that a rapidly rotating ellipsoidal core of a higher density is formed in the initial stage of the merger. Irrespective of the used model, however, these results apparently indicate that a merger between two relativistic clusters is an efficient source of gravitational waves.

§6. Summary

We have performed fully general relativistic simulations of the merger between relativistic clusters of collisionless particles adopting a new spatial gauge, the AMD (approximate minimum distortion) gauge condition. We have reached the following conclusions:

- By using the AMD gauge condition, it is possible to perform numerical simulations of coalescing binary clusters for a time much longer than the dynamical time scale of the system when the merger does not produce a black hole. Also, it is found that with this gauge condition, gravitational waveforms can be calculated fairly accurately. These results suggest that with the AMD gauge condition, the spatial coordinate distortion is suppressed to a level adequate to carry out stable and accurate simulations.
- Our AMD gauge condition, as well as a class of spatial gauge conditions similar to the MD gauge conditions, still has an undesirable, coordinate spreading property (i.e., $\beta^r > 0$) when applying it to the study of black hole formation. As a result of this property, the spatial resolution around a black hole forming region rapidly tends to become insufficient.
- However, if our AMD gauge condition is slightly modified during the process of black hole formation, it is still possible to carry out simulations up to the formation of an apparent horizon. Using this approach, we have shown that it is possible to perform numerical simulations over a sufficient long time scale from the early merging phase up to the formation of a black hole.
- In a merger between two highly relativistic star clusters with $M_*/r_0 = 1/4$ into a new cluster, the amplitude of gravitational waves has been estimated as $\sim 10^{-18}(M/10^6\,M_\odot)$ at a distance of $\sim 4000\,\mathrm{Mpc}$ with a frequency $\sim 10^{-2}(10^6\,M_\odot/M)\,\mathrm{Hz}$. Also, $\sim 0.5\%$ of the rest mass energy may be dissipated by gravitational waves in the final phase of the coalescence.

The spatial gauge conditions presented and investigated in this paper are useful for a wide variety of problems, and we expect that they will be widely exploited for performing simulations of coalescing binary neutron stars, which represent the most promising sources of gravitational waves for kilometer-size laser interferometers. When a general relativistic hydrodynamic code is installed to replace numerical code for collisionless particles, we will be able to perform the numerical simulations for such binary systems and follow them up to the formation of black holes or new rotating neutron stars. This work is now in progress, and in future papers we will present the numerical results. [22)]

Acknowledgements

The author thanks T. Nakamura, M. Sasaki, S. Shapiro and L. Rezzolla for frequent helpful conversations. He also thanks L. Rezzolla for carefully reading the manuscript and for providing helpful comments. Numerical computations were performed on the FACOM VX/4R machine in the data processing center of the

National Astronomical Observatory of Japan (NAOJ). This work was supported by a Grant-in-Aid (Nos. 08NP0801 and 09740336) of the Japanese Ministry of Education, Science, Sports and Culture, and JSPS Fellowships for Research Abroad.

Appendix A
—— *Numerical Treatment for the Transport Terms* ——

For treating the transport terms in the evolution equations of geometric variables, we use a method similar to that adopted by Stark and Piran.[23] In the following, we demonstrate the treatment only in the x direction, but the same operations are also carried out in the y and z directions. We also assume a uniform grid along the x direction and denote the grid spacing and time step as δx and δt.

Evolution equations for the geometric variables may be written in the form

$$(\partial_t - \beta^x \partial_x) Q = S, \tag{A·1}$$

where Q denotes one of the geometric variables and S denotes the source term. The solution for the finite difference equation is written

$$Q_i^{n+1} = Q_i^n - \frac{1}{2}\Big[\nu(Q_{i+1}^n - Q_{i-1}^n) - |\nu|(Q_{i+1}^n - 2Q_i^n + Q_i^n)\Big] + S_i^{n+1/2}\delta t, \tag{A·2}$$

in the first order upwind scheme, and

$$Q_i^{n+1} = Q_i^n - \frac{1}{2}\Big[\nu(Q_{i+1}^n - Q_{i-1}^n) - \nu^2(Q_{i+1}^n - 2Q_i^n + Q_{i-1}^n)\Big] + S_i^{n+1/2}\delta t, \tag{A·3}$$

in the second order scheme. Here, $\nu = -(\beta^x)_i^{n+1/2}\delta t/\delta x$, and Q_i^n denotes Q at the n-th time step and i-th grid point. In this paper, we compute Q_i^{n+1} as

$$\begin{aligned} Q_i^{n+1} = Q_i^n - \frac{1}{2}\Big[&\nu(Q_{i+1}^n - Q_{i-1}^n) - (1-s_i)|\nu|(Q_{i+1}^n - 2Q_i^n + Q_{i-1}^n) \\ &- s_i\nu^2(Q_{i+1}^n - 2Q_i^n + Q_{i-1}^n)\Big] + S_i^{n+1/2}\delta t. \end{aligned} \tag{A·4}$$

Here, s_i is a limiter function at the i-th grid point, chosen as

$$s_i = \begin{cases} \dfrac{2\delta Q_i \delta Q_{i-1} + \epsilon}{\delta Q_i^2 + \delta Q_{i-1}^2 + \epsilon} & \text{for } \delta Q_i \delta Q_{i-1} \geq 0, \\ 0 & \text{for } \delta Q_i \delta Q_{i-1} < 0, \end{cases} \tag{A·5}$$

where $\delta Q_i = Q_{i+1}^n - Q_i^n$ and ϵ is an appropriately small constant.

Appendix B
—— *Behavior of F_i in Our AMD Gauge* ——

Substituting Eq. (3·8) into Eq. (2·20), we obtain

$$(\partial_t - \beta^k \partial_k) F_i = 2\alpha\left(f^{kj}\tilde{A}_{ik,j} + f^{kj}{}_{,j}\tilde{A}_{ik} - \frac{1}{2}\tilde{A}^{jl}h_{jl,i}\right) + 2f^{jk}\alpha_{,k}\tilde{A}_{ij}$$

$$+\delta^{jl}\beta^{k}{}_{,l}(h_{ij,k}+h_{ik,j})+h_{il}\beta^{l}{}_{,jk}\delta^{jk}+F_l\beta^{l}{}_{,i}+h_{jl}\beta^{l}{}_{,ik}\delta^{jk}$$
$$-\frac{2}{3}(F_i\beta^{l}{}_{,l}+h_{ij}\beta^{l}{}_{,lk}\delta^{jk})$$
$$\equiv S_i^F. \qquad \text{(B·1)}$$

Here S_i^F is a nonlinear function and can be set to zero in the linear approximation. Hence, in this approximation, F_i is always zero if it is zero initially. Even when we consider a linear perturbation in the Schwarzschild spacetime or the spacetime of a spherical star, S_i^F is non-linear and F_i is always zero if initially zero. However, in a spacetime of a rotating black hole or star, h_{ij} (f^{ij}), β^k and $\tilde{A}_{ij}$ appear at zeroth order, so F_i also appears from zeroth order. Nevertheless, in the case that the rotation of the object is not very rapid, h_{ij} (f^{ij}), β^k and $\tilde{A}_{ij}$ are small, and hence F_i can be considered to be small. Even in the case that the object is rapidly rotating, h_{ij} (f^{ij}), β^k and $\tilde{A}_{ij}$ quickly decay as $O(r^{-2})$, $O(r^{-2})$ and $O(r^{-3})$, respectively, so that S_i^F and F_i can still be regarded as small quantities everywhere except near the rapidly rotating object. Furthermore, in the post-Newtonian approximation, S_i^F contains at most third post-Newtonian quantities, because h_{ij} (f^{ij}), β^i and $\tilde{A}_{ij}$ can be regarded as the second, first and first post-Newtonian quantities, respectively.[16),17)] Thus, except in the highly relativistic region in which h_{ij}, β^i and $\tilde{A}_{ij}$ become $O(1)$ or a relativistic region near the rapidly rotating relativistic objects, S_i^F is guaranteed to be small, and hence, F_i is expected to be small as long as it is small enough on an initial time slice (i.e., as long as we do not consider strange initial conditions in which F_i is large initially).

References

1) A. Abramovici et al., Science **256** (1992), 325.
2) K. S. Thorne, in *Proceeding of Snowmass 94 Summer Study on Particle and Nuclear Astrophysics and Cosmology*, ed. E. W. Kolb and R. Peccei (World Scientific, Singapore, 1995).
3) C. Bradaschia et al., Nucl. Instrum. and Methods **A289** (1990), 518.
4) J. Hough, in *Proceedings of the Sixth Marcel Grossmann Meeting*, ed. H. Sato and T. Nakamura (World Scientific, Singapore, 1992), p. 192.
5) K. Kuroda et al., in *Proceedings of International Conference on Gravitational Waves: Sources and Detectors*, ed. I. Ciufolini and F. Fidecaro (World Scientific, Singapore, 1997), p. 100.
6) For example, http://lisa.jpl.nasa.gov/. See also, Ref. 2).
7) For example, L. Blanchet, in *Relativistic gravitation and gravitational radiation*, ed. J.-P. Lasota and J.-A. Marck (Cambridge University Press, Cambridge, 1997), see also references cited therein.
8) For example, see K. Oohara and T. Nakamura, in *Relativistic gravitation and gravitational radiation*, ed. J.-P. Lasota and J.-A. Marck (Cambridge University Press, Cambridge, 1997), p. 309.
   As for a USA project, see, http://www.npac.syr.edu/projects/bh.
9) L. Smarr and J. W. York, Phys. Rev. **D17** (1978), 1945, 2529.
10) M. Shibata, Prog. Theor. Phys. **101** (1999), 251.
11) For example, M. C. Begelman and M. J. Rees, Mon. Not. R. Astron. Soc. **185** (1978), 847.
12) M. Shibata and T. Nakamura, Phys. Rev. **D52** (1995), 5428.
13) We should mention that Nakamura first pointed out the importance and usefulness of the introduction of F_i more than 10 years ago. See, T. Nakamura et al., Prog. Theor. Phys. Suppl. No. 90 (1987), 76.
14) M. Shibata, Phys. Rev. **D55** (1997), 2002.

15) For example, M. Shibata, Phys. Rev. **D55** (1997), 6019.
M. Shibata, K. Oohara and T. Nakamura, Prog. Theor. Phys. **98** (1997), 1081.
M. Shibata, T. W. Baumgarte and S. L. Shapiro, Phys. Rev. **D58** (1998), 023002.
16) h_{ij} and β^i are the second and first post-Newtonian quantities, respectively, if F_i is higher than third post-Newtonian order. In the present AMD gauge condition, F_i can be regarded as a third post-Newtonian quantity (see Appendix B), so that h_{ij} and β^i are actually the second and first post-Newtonian order. This fact can be found by performing a post-Newtonian analysis in the (3+1) formalism as we have done in the next reference 17).
17) H. Asada, M. Shibata and T. Futamase, Prog. Theor. Phys. **96** (1996), 81.
18) V. Moncrief, Ann. of Phys. **88** (1974), 323. The Moncrief variables are defined in a Schwarzschild spacetime. In this paper, we use them by simply setting the gravitational mass to be zero in order to consider the gauge invariant quantities in the flat spacetime.
19) For example, S. L. Shapiro and S. A. Teukolsky, *Black Holes, White Dwarfs, and Neutron Stars* (New York, Wiley, 1983), chapter 16.
20) This feature has been already found by the following authors in a semi-analytical study of the Oppenheimer-Snyder collapse in the MD gauge and maximal slice conditions. L. I. Petrich, S. L. Shapiro and S. A. Teukolsky, Phys. Rev. **D31** (1985), 2459, see Fig. 2 in this paper.
21) M. Berger and J. Oliger, J. Comp. Phys. **53** (1984), 484.
22) M. Shibata, in preparation.
23) R. F. Stark and T. Piran, Comp. Phys. Rep. **5** (1987), 221.